

Building up JWST-SUSPENSE: inside-out quenching at cosmic noon from age, Fe-, and Mg-abundance gradients

Chloe M. Cheng^{1,*}, Martje Slob¹, Mariska Kriek¹, Aliza G. Beverage², Guillermo Barro³, Rachel Bezanson⁴, Anna de Graaff⁵, Natascha M. Förster Schreiber⁶, Brian Lorenz², Danilo Marchesini⁷, Ignacio Martín-Navarro^{8,9}, Adam Muzzin¹⁰, Andrew B. Newman¹¹, Sedona H. Price¹², Katherine A. Suess¹³, Arjen van der Wel¹⁴, Jesse van de Sande¹⁵, Pieter G. van Dokkum¹⁶, and Daniel R. Weisz²

¹ Leiden Observatory, Leiden University, P.O. Box 9513, 2300 RA Leiden, The Netherlands

² Department of Astronomy, University of California, Berkeley, CA 94720, USA

³ University of the Pacific, Stockton, CA 90340 USA

⁴ Department of Physics & Astronomy and PITT PACC, University of Pittsburgh, Pittsburgh, PA 15260, USA

⁵ Max-Planck-Institut für Astronomie, Königstuhl 17, D-69117, Heidelberg, Germany

⁶ Max-Planck-Institut für extraterrestrische Physik, Giessenbachstrasse 1, D-85748 Garching, Germany

⁷ Department of Physics & Astronomy, Tufts University, MA 02155, USA

⁸ Instituto de Astrofísica de Canarias, c/Vía Láctea s/n, E38205 - La Laguna, Tenerife, Spain

⁹ Departamento de Astrofísica, Universidad de La Laguna, E-38205 La Laguna, Tenerife, Spain

¹⁰ Department of Physics and Astronomy, York University, 4700 Keele Street, Toronto, Ontario, ON M3J 1P3, Canada

¹¹ Observatories of the Carnegie Institution for Science, 813 Santa Barbara Street, Pasadena, CA 91101, USA

¹² Space Telescope Science Institute (STScI), 3700 San Martin Drive, Baltimore, MD 21218, USA

¹³ Department for Astrophysical & Planetary Science, University of Colorado, Boulder, CO 80309, USA

¹⁴ Sterrenkundig Observatorium, Universiteit Gent, Krijgslaan 281 S9, B-9000 Gent, Belgium

¹⁵ School of Physics, University of New South Wales, Sydney, NSW 2052, Australia

¹⁶ Astronomy Department, Yale University, 52 Hillhouse Avenue, New Haven, CT 06511, USA

Received XXX; accepted XXX

ABSTRACT

Spatially resolved stellar populations of massive, quiescent galaxies at cosmic noon provide powerful insights into star-formation quenching and stellar mass assembly mechanisms. Previous photometric work has revealed that the cores of these galaxies are redder than their outskirts. However, spectroscopy is needed to break the age-metallicity degeneracy and uncover the driver of these colour gradients. Here, we derive age and elemental abundance gradients for 8 distant ($1.2 \lesssim z \lesssim 2.2$), massive ($10.3 \lesssim \log(M_*/M_\odot) \lesssim 11.1$), quiescent galaxies, by fitting full-spectrum models to ultra-deep NIRSpec-MSA spectroscopy from the JWST-SUSPENSE survey. We find that these galaxies have negative age, positive [Mg/H] and [Mg/Fe], and flat [Fe/H] gradients, implying that galaxy cores are older and Mg-deficient compared to galaxy outskirts. The age gradients indicate inside-out quenching, while the Mg-deficient cores suggest rapid gas expulsion as the central quenching mechanism. Thus, galaxy cores formed faster and quenched more efficiently than their outskirts. In this scenario, however, our [Fe/H] and [Mg/Fe] gradients are still puzzling. Our results contrast lower-redshift studies, which find flat age and [Mg/Fe] gradients and negative metallicity gradients. Additionally, we find a positive trend between age gradients and rotational support, and marginal trends between gradients and galaxy velocity dispersions and ages. We discuss our findings in the context of galaxy growth scenarios, including minor mergers and progenitor bias, and the possible occurrence of different quenching mechanisms across redshift. With this work, we present the first stellar population gradients from NIRSpec-MSA spectroscopy, in the largest current sample of distant, quiescent galaxies.

Key words. Galaxies: abundances – Galaxies: evolution – Galaxies: formation – Galaxies: stellar content

1. Introduction

Spatially resolved measurements of stellar populations are critical for our understanding of galaxy assembly histories and star-formation quenching mechanisms. In the local Universe, key insights into the formation and assembly of massive, early-type galaxies have been gained by measuring stellar population gradients out to large radii (e.g. [Peletier & Valentijn 1989](#); [Franx & Illingworth 1990](#); [Kuntschner et al. 2006](#); [Goddard et al. 2017](#); [Li et al. 2018](#); [Santucci et al. 2020](#); [Parikh et al. 2024](#)). In particular, findings of flat α -element abundance gradients, flat or mildly

positive age gradients, and mildly negative metallicity gradients (implying iron-rich cores) suggest that these galaxies have experienced inside-out growth via galaxy mergers (e.g., [Mehlert et al. 2003](#); [La Barbera et al. 2005](#); [Greene et al. 2013, 2015](#); [Greene et al. 2019](#); [Martín-Navarro et al. 2018](#); [Zibetti et al. 2020](#)).

Advancements in observations and modeling have allowed these measurements to be extended to higher redshifts (z). Specifically, negative colour gradients (e.g., [Wuyts et al. 2010](#); [Ciocca et al. 2017](#); [Suess et al. 2019a,b, 2020, 2021](#); [Miller et al. 2023](#); [van der Wel et al. 2024](#)), flat age and α -element abundance gradients, and negative metallicity gradients contribute to the inside-out growth picture out to $z \sim 1$ ([Cheng et al. 2024](#), see also [Franx et al. 2008](#); [van Dokkum et al. 2015](#); [D'Eugenio](#)

* E-mail: cheng@strw.leidenuniv.nl (CMC)

et al. 2020). In this scenario, the outskirts are built up by the accretion of low metallicity (i.e., bluer) stellar populations via minor mergers. However, progenitor bias, where quiescent galaxy population growth is driven by contributions of larger galaxies at later times (van Dokkum & Franx 2001; Carollo et al. 2013; Poggianti et al. 2013; Keating et al. 2015; Damjanov et al. 2019, 2023), may also explain the observed gradients at $z \gtrsim 0$.

The stellar populations of analogous galaxies at even earlier times may conceal important clues, allowing us to reveal this primary mode of galaxy assembly. Specifically, in the hierarchical model of galaxy formation, the compact central cores of massive galaxies are formed at cosmic noon ($z \sim 2 - 3$) or earlier, with their outer wings being built up by accretion of low-mass satellite galaxies towards $z \sim 0$ (Bezanson et al. 2009; Hopkins et al. 2009; Oser et al. 2010; van Dokkum et al. 2014; Rodriguez-Gomez et al. 2016). High-resolution photometric studies beyond $z \sim 1$ may support this scenario, with colour gradients strengthening over time. These colour gradients suggest that the compact, red cores of galaxies accrete bluer, low-mass satellites (e.g., Wuyts et al. 2010; Szomoru et al. 2013; Ciocca et al. 2017; Suess et al. 2019b, 2020, 2021, 2023; Miller et al. 2022, 2023, although see Pizzardo et al. 2025), but they could also be signatures of inside-out quenching (e.g., Suess et al. 2019a). In the former scenario, the gradients would reflect metallicity, while in the latter, age would drive the observed colours. Furthermore, dust could also play a role, as age, metallicity and dust are strongly degenerate in broadband spectral energy distributions (Worley 1994; Bell & de Jong 2001; Bruzual & Charlot 2003; Gallazzi et al. 2005; Leja et al. 2019). Thus, in order to understand the main mechanism by which galaxies build up their stellar mass, we need to determine which physical property may be driving the observed colour gradients.

To isolate the dominant driver of massive galaxy growth, we must measure robust stellar population gradients in massive, quiescent galaxies out to at least $z \sim 2$, before the majority of quenching and growth began (Oser et al. 2010; Rodriguez-Gomez et al. 2016; Whitaker et al. 2012). To achieve this goal, we require deep, spatially-resolved, rest-frame optical spectra of a sample of massive, quiescent galaxies, to obtain detailed measurements of absorption lines. However, these measurements are extremely challenging beyond the local Universe. Thus, only a handful of varying spectroscopic gradient measurements exist, for a small number of relatively young quiescent galaxies beyond $z \sim 1$. For example, Jafariyazani et al. (2020) found a flat age and [Mg/Fe] gradient and a slightly negative [Fe/H] gradient in a massive, lensed galaxy at $z \sim 2$ using deep MOSFIRE spectra. Ditrani et al. (2022) used *Hubble Space Telescope* (HST) grism spectra and found negative metallicity and diverse age gradients in 4 distant, quiescent galaxies. Akhshik et al. (2023) examined similar data and found diverse age and metallicity gradients in 8 galaxies. However, due to line blending, metallicities obtained from low-resolution spectroscopy ($R \sim 100$) may be highly uncertain ($\sim 0.3 - 0.5$ dex, Akhshik et al. 2023).

Detailed stellar population maps have also been achieved with *James Webb Space Telescope* (JWST) integral field unit (IFU) spectroscopy, but only for very young, individual, quiescent galaxies. For example, Pérez-González et al. (2024) examined a massive galaxy at $z \sim 3.7$ and found a strongly negative total metallicity gradient, a slightly negative age gradient, and a slightly positive dust gradient. Additionally, D'Eugenio et al. (2024) examined a galaxy at $z \sim 3$ and found a flat age gradient. Thus, to come to a consensus about the behaviour of spatially resolved stellar populations in distant, quiescent galaxies, we need larger samples that also include older, fainter galaxies.

Table 1. Our sample of massive quiescent galaxies from JWST-SUSPENSE.

ID	$z_{\text{spec}}^{\text{a}}$	$\log(M_*)^{\text{a}}$	Kinematic Properties ^b		R_e^{b}
			V_{r_e}/σ_0	σ_0 (km/s)	
130040	1.170	11.1	$0.63^{+0.06}_{-0.07}$	285^{+5}_{-5}	0.62 ^c
127345	1.171	10.7	-	-	0.18 ± 0.08
127154	1.205	10.8	-	242^{+4}_{-6}	0.25 ± 0.05
127108	1.335	10.3	$0.54^{+0.12}_{-0.20}$	210^{+5}_{-10}	0.17 ± 0.08
129149	1.578	11.0	$0.49^{+0.07}_{-0.12}$	387^{+4}_{-34}	0.12 ± 0.01
128041	1.760	10.7	$1.48^{+0.07}_{-0.06}$	226^{+1}_{-1}	0.19 ± 0.05
129133	2.139	11.1	$1.19^{+0.07}_{-0.07}$	257^{+2}_{-1}	0.19 ± 0.10
128036	2.196	11.0	$1.18^{+0.09}_{-0.08}$	210^{+3}_{-6}	0.13 ± 0.03

^a Presented in Slob et al. (2024).

^b Presented in Slob et al. (2025).

^c Presented in Griffith et al. (2012).

ies. While JWST-IFU observations like those in Pérez-González et al. (2024) and D'Eugenio et al. (2024) are ideal, it is prohibitively expensive to obtain these data for larger samples.

To avoid the expense of IFU observations, we can take advantage of the micro shutter assembly (MSA), JWST's multi-object spectrometer on the Near Infrared Spectrograph (NIRSpec). This has been achieved with the JWST-Spectroscopic Ultradeep Survey Probing Extragalactic Near-infrared Stellar Emission (SUSPENSE), an ultra-deep spectroscopic survey of 20 quiescent galaxies at $1 \lesssim z \lesssim 3$ (Slob et al. 2024). SUSPENSE leverages the NIRSpec-MSA to achieve both medium spectral and moderate spatial resolutions for many galaxies in a single pointing. In this work, we take advantage of the unique capabilities of this instrument to present robust, spatially resolved measurements of age, [Fe/H], [Mg/Fe], and [Mg/H] in a sample of 8 massive, quiescent galaxies at $1.2 \lesssim z \lesssim 2.2$ from SUSPENSE.

This paper is organised as follows: in Section 2 we describe the spectroscopic data from SUSPENSE and our sample selection. In Section 3 we outline our methods to correct spectral resampling artifacts, extract spatially resolved spectra, determine de-projected distances, and measure spatially resolved stellar population parameters. In Section 4 we present our resulting gradients. We discuss our results and their implications for galaxy quenching mechanisms and assembly histories in Section 5 and present our conclusions in Section 6. Throughout, we assume a flat Λ CDM cosmology with $\Omega_m = 0.3$, $\Omega_\Lambda = 0.7$, and $H_0 = 70 \text{ km s}^{-1} \text{ Mpc}^{-1}$ and a Kroupa (2001) initial mass function (IMF). All magnitudes are given in the AB-magnitude system (Oke & Gunn 1983).

2. Data and sample

The spectroscopic data in this work are drawn from JWST-SUSPENSE¹ (ID: 2110², PIs: Kriek and Beverage), an ultra-deep (16.4 hours on-source), NIRSpec-MSA/G140M-F100LP ($R \sim 1300$) survey of 20 massive, quiescent galaxies at $1 \lesssim z \lesssim 3$ (Slob et al. 2024, see also Beverage et al. 2025). Targets were identified from the UltraVISTA (McCracken et al. 2012) K-band DR3 catalogue (Muzzin et al. 2013b), and were selected to be quiescent using the Muzzin et al. (2013a) UVJ classification. The SUSPENSE galaxies were observed at two dither configura-

¹ <https://suspense.strw.leidenuniv.nl/>.

² doi:10.17909/y6rb-fn24.

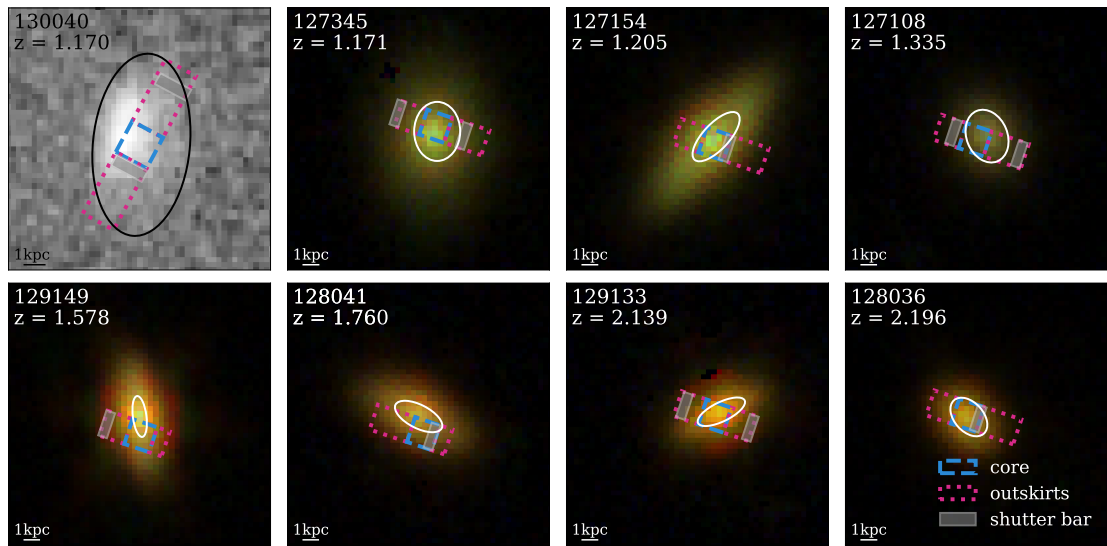


Fig. 1. Colour image cutouts of the 8 distant, quiescent galaxies in our sample. Seven galaxies have NIRCam imaging, which we combine into RGB images here. Galaxy 130040 does not have NIRCam imaging, so we show a cutout of the COSMOS *HST*/ACS F814W image (Koekemoer et al. 2007; Scoville et al. 2007, note that this image is rotated by 90 degrees compared to the NIRCam images). We highlight the regions that we combine for the core and outskirt spectra in blue and pink, respectively (see Section 3.2). We also indicate where shutter bars lie within these core and outskirt regions with shaded rectangles. We indicate $1 R_e$ in convolved space for each galaxy with an ellipse (see Section 3.3).

tions, by offsetting two nearly identical MSA configurations by 8 shutters in the dispersion direction. Due to micro shutter defects, it was not possible to open the exact same shutters in both configurations for all targets. Thus, a small number of galaxies were observed in different positions in each configuration (see Section 3.2). A two-point nod pattern was also implemented for each galaxy, with a two-micro-shutter cross-dispersion offset to avoid self-subtraction of the extended targets during the data reduction. After identifying the optimal configuration, the standard three-shutter slitlets were extended by hand where possible, ranging from 3 to 7 micro shutters in length. Filler star-forming targets were also added to the configuration. The "unconstrained" (mid-bar) option was implemented for the source centring constraint, and thus some galaxies are centred behind MSA bars (see Fig. 1). The data were reduced via a customised version of v1.12.5 of the *JWST* Science Calibration Pipeline (Bushouse et al. 2023) and version 1183 of the Calibration Reference Data System (CRDS). See Slob et al. (2024) for details.

We select a subset of the quiescent galaxies from SUSPENSE. In particular, we require each spectrum (integrated, core, and outskirts, see Section 3.2) to have a rest-frame S/N $\gtrsim 20 \text{ \AA}^{-1}$ between $4520 - 4820 \text{ \AA}$ (the region that all spectra have in common) to derive robust stellar population parameters (we determine these limits by performing tests with simulated observations, similar to Cheng et al. 2024). Additionally, we discard four galaxies, due to insufficient wavelength coverage (IDs 129982 and 130208), or due to the presence of strong emission lines that may be associated with active galactic nuclei (AGN, IDs 128452 and 130647, see also Beverage et al. 2025). Our selection does not lead to a bias in mass, size, or integrated age compared to the total SUSPENSE quiescent sample.

Image cutouts of our final sample of 8 quiescent galaxies (40% of the total quiescent SUSPENSE sample) are shown in Fig. 1. Seven galaxies have *JWST*/Near Infrared Camera (NIRCam) imaging from the Cosmological Evolution Survey (COSMOS)-Web survey (Casey et al. 2023). We obtain these images from the Cosmic Dawn Centre (DAWN) *JWST* Archive

(DJA³, see Brammer 2023 and Valentino et al. 2023) and combine the F115W, F277W, and F444W data into RGB images using the ASTROPY make_lupton_rgb function (this applies an inverse hyperbolic sine scaling, Lupton et al. 2004; Astropy Collaboration et al. 2022). Galaxy 130040 does not have NIRCam imaging, so we show the COSMOS *HST*/Advanced Camera for Surveys (ACS) F814W image (Koekemoer et al. 2007; Scoville et al. 2007). We report properties of our sample in Table 1.

3. Methods

3.1. Correction of resampling noise

Spatially resolved observations obtained with *JWST* are affected by undersampling of the point spread function (PSF). This undersampling produces an artifact called "resampling noise", which presents itself as periodic flux variations as a function of wavelength (Smith et al. 2007; Law et al. 2023; Perna et al. 2023; Dumont et al. 2025; Newman et al. 2025). These variations are colloquially referred to as "wiggles". This behaviour has been observed in the previous generation of space-based telescopes (see, e.g., Dressel et al. 2007; Smith et al. 2007; Anderson 2016), and in *JWST* IFU instruments (e.g., Law et al. 2023; Perna et al. 2023; Dumont et al. 2025; Newman et al. 2025). We also observe these wiggles in the individual spectral rows of the SUSPENSE NIRSpec-MSA 2D spectra. The wiggles do not strongly affect integrated observations, as they are averaged out when the flux is integrated over large apertures (see Appendix A and Law et al. 2023; Perna et al. 2023; Newman et al. 2025). However, the wiggles are a significant concern for spatially-resolved studies as they can affect the shapes of continua and broad spectral features, potentially biasing spectral modelling (Perna et al. 2023). We correct the wiggles by implementing an algorithm based on those presented by Perna et al. (2023)⁴ and Dumont

³ <https://dawn-cph.github.io/dja/index.html>.

⁴ https://github.com/micheleperna/JWST-NIRSpec_wiggles.

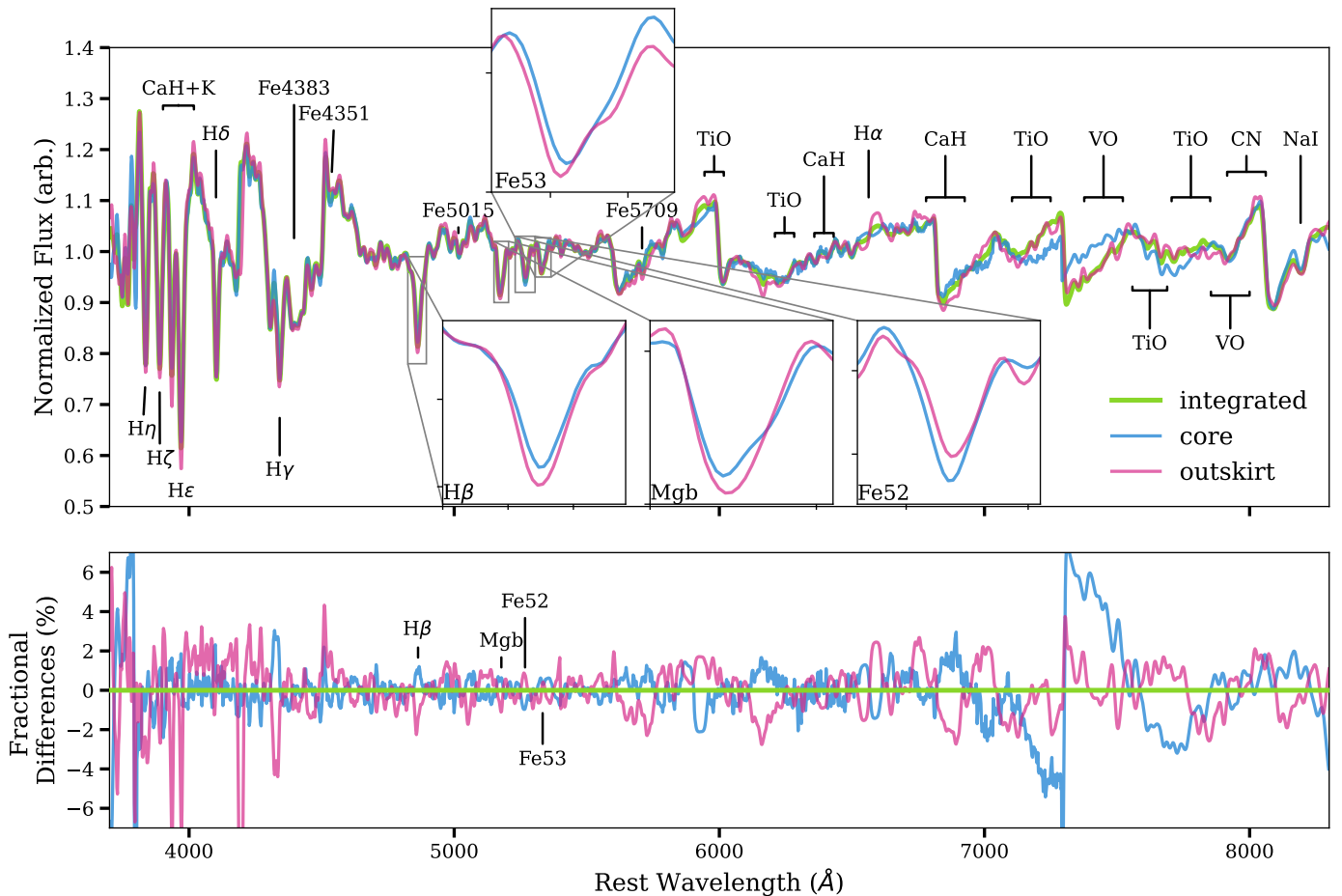


Fig. 2. *Top:* Stack of continuum-normalized spectra of all galaxies. The integrated stack is shown in green, the core stack is shown in blue, and the outskirt stack is shown in magenta. We label key spectral features. In the inset panels, we zoom-in on the $H\beta$ ($\sim 4849 - 4878 \text{ \AA}$, sensitive to age), Mgb ($\sim 5162 - 5194 \text{ \AA}$, sensitive to $[\text{Mg}/\text{H}]$), $Fe52$ ($\sim 5247 - 5287 \text{ \AA}$, sensitive to age and $[\text{Fe}/\text{H}]$), and $Fe53$ ($\sim 5314 - 5454 \text{ \AA}$, sensitive to age and $[\text{Fe}/\text{H}]$) features in the core and outskirt spectra. *Bottom:* The fractional differences of each stacked spectrum, where we divide each spectrum by the stacked integrated spectrum.

et al. (2025)⁵, customising these routines for our specific case. See Appendix A for details.

3.2. Spectral extraction

For each galaxy, we apply a custom extraction routine to the wiggle-corrected 2D spectrum to obtain three 1D spectra: an integrated spectrum and spectra in two spatial bins (representing the core and outskirts). We follow a similar procedure as Cheng et al. (2024), but modified for our data. We describe our extraction routine here.

We obtain the flux profile of each galaxy by collapsing the 2D spectrum over the wavelength axis. We fit a Moffat (1969) profile to each flux profile, as in Cheng et al. (2024). We use the Moffat profile to identify spectral rows with significant flux (rows that are approximately between the 3rd and 97th percentiles of the Moffat profile). We disregard all rows outside of the 3rd and 97th percentiles, as Cheng et al. (2024) found that using this region resulted in a minimum difference in S/N between the core and outskirt spectra. We also find that including these outer rows lowers the S/N.

To extract the integrated spectrum, we sum the rows between the 3rd and 97th percentiles. For the spatially binned spectra, we

take the brightest two rows to comprise the "core" of the galaxy and sum these together. The remaining rows comprise the "outskirts" of the galaxy and are similarly summed. We note that Cheng et al. (2024) split the spectral rows into sub-rows to capture the precise region between the 3rd and 97th percentiles of the Moffat profile, and to define the core of the galaxy as the middle 30% of the profile. We do not split our spectral rows, as the spatial undersampling of NIRSpec makes neighboring rows largely (though not completely) independent. Additionally, Cheng et al. (2024) performed an optimal extraction by weighting the spectral rows by the Moffat profile before summing. We do not apply an optimal extraction, so as to not down weigh the lower-signal outer rows.

As the SUSPENSE galaxies were observed using two dither configurations (see Section 2 and Slob et al. 2024), there are two 2D spectra for each galaxy. We perform the extraction routine described above on the 2D spectrum in each dither, giving us an integrated, core, and outskirt spectrum for each dither. We mask outliers in the flux due to cosmic ray impacts or bad pixels using the outlier detection algorithm from Slob et al. (2024). For seven galaxies, the dithers encompass the same spatial regions. In these cases, we mean-stack the integrated, core, and outskirt spectra for each dither, respectively, leaving us with three 1D spectra (one integrated, core, and outskirt spectrum for each galaxy).

⁵ <https://github.com/antoinedumontneira/WICKED>.

The two dithers for the remaining galaxy (130040) were performed in different positions on the galaxy as its centre was exactly between two shutters, and thus each dither encloses a different spatial region. Therefore, for 130040 only, we analyse the core and outskirt spectra for each dither separately. After fitting (see Section 4), we find large error bars on our results in dither 1, so we discard it from the analysis and only consider dither 2. We show our defined core and outskirts regions for each galaxy in Fig. 1 (with only the dither 2 regions shown for 130040).

We show a representation of the integrated, core, and outskirt spectra in Fig. 2. We stack all of our extracted, continuum-normalised (where we divide by a 7th order polynomial), rest-frame integrated, core, and outskirt spectra, respectively, by resampling the spectra to the same wavelength array via SPEC-TRES (Carnall 2017), normalizing them by the region between 5200 – 5600 Å, and smoothing them to the maximum velocity dispersion of our sample ($\sigma \sim 390$ km s $^{-1}$). We also show the fractional differences in the bottom panel. The three spectra have visible variations relative to each other⁶. To emphasise these differences, we zoom in on the H β , Mgb, Fe52, and Fe53 strong absorption features. The four features demonstrate significant differences between the core and outskirts. The H β feature is largely sensitive to age, indicating that the average core stellar population has a different age compared to the average outskirt stellar population. The Fe52 and Fe53 features are mainly sensitive to [Fe/H], but are also affected by age due to the age-metallicity degeneracy (Worthey 1994; Bruzual & Charlot 2003; Gallazzi et al. 2005). Interestingly, the differences between the core and the outskirt spectra are opposite in these two features (i.e. Fe52 is stronger in the core while Fe53 is stronger in the outskirts). Meanwhile, the Mgb feature is sensitive to [Mg/H], indicating that the Mg abundances of the core and outskirt stellar populations are different. We discuss this further in Section 4.

3.3. Determining distances and radii

In order to present our spatially resolved measurements as a function of radius, there are several factors that we must account for, including (i) the convolved nature of the observations, (ii) the fact that our galaxies may be elliptical in shape, and (iii) the arbitrary location of the micro shutters on each galaxy.

First, our observations are blurred due to convolution with the NIRSpec PSF. To account for this, we derive the convolved R_e for each galaxy. We use a similar method to those presented in Price et al. (2016) and Cheng et al. (2024), where the intrinsic R_e , measured by fitting images with GALFIT (Peng et al. 2010) is also convolved with the NIRSpec PSF. Specifically, we take the structural GALFIT parameters measured from JWST/NIRCam F150W images by Slob et al. (2025) (or those measured from COSMOS HST/ACS F814W images by Griffith et al. 2012 for 130040) and use these parameters to create an intrinsic galaxy image in GALFIT for each galaxy. We create these images at an increased spatial resolution (0.05'' per pixel) compared to our observations. We convolve each mock galaxy image with the NIRSpec-MSA PSF, generated with STPSF⁷ (Perrin et al. 2015), keeping all shutters open⁸. We perform aperture sums on a series of circular aper-

tures of increasing size that we place on the convolved model image using PHOTUTILS (Bradley et al. 2024), and determine the radius enclosing 50% of the light for the convolved model. We determine the factor by which this convolved R_e differs from the intrinsic GALFIT R_e from Slob et al. (2025) (or Griffith et al. 2012 for 130040) and apply this factor to the GALFIT semimajor axis (b) to obtain a similarly convolved b .

To determine the average distance to the centre for our core and outskirt regions in units of convolved R_e , we must also consider that our galaxies are elliptical in shape on the sky, and are not perfectly round. Additionally, we must take into account the arbitrary placement of the micro shutters on each galaxy, which are typically not centered or aligned along the major axis. To achieve this, we first determine the location of each spectral row on the sky. We divide each row into ~ 45000 subpixels, by interpolating the coordinates of each row, and assuming each row is represented by a rectangle of width 0.1'' (the MSA pixel scale) and height 0.2'' (the open width of a micro shutter, Ferruit et al. 2022). We generate a series of ellipses with increasing R_e and b centred on the target galaxy, maintaining the axis ratio. Note that we disregard the effect of the PSF on the ellipticity, and that smaller, inner ellipses will become rounder than outer ellipses. We determine the R_e of each subpixel from the dimensions of the respective intersecting ellipse. The R_e of that pixel is then the median R_e of all of the subpixels in the row. To determine the average R_e of each spatial bin, we take the weighted mean of the R_e of the rows in each region (core and outskirts), using the flux of each row as the weights. Finally, we take the mean of the R_e in each of the two observed dithers to get the final de-projected distance to the core and outskirts in units of convolved R_e . The dithers are at approximately the same position on each galaxy (other than for 130040, see above), but we take the mean of the R_e in each dither to account for minor positional deviations.

3.4. Full spectrum fitting

We fit the spectra using ALF α ⁹ (Beverage 2024; Beverage et al. 2025), a Python version of the ABSORPTION LINE FITTER (ALF¹⁰, Conroy & van Dokkum 2012; Conroy et al. 2018). The ALF and ALF α models are built on empirical simple stellar populations (SSPs), constructed using the Mesa Isochrones and Stellar Tracks (MIST, Choi et al. 2016) and the Spectral Polynomial Interpolator¹¹ (SPI, Villaume et al. 2017). ALF and ALF α make use of stellar libraries, including the Medium Resolution INT Library of Empirical Spectra (MILES, Sánchez-Blázquez et al. 2006), the Extended Infrared Telescope Facility stellar library (E-IRTF, Villaume et al. 2017), the Mann et al. (2015) sample of M-dwarf spectra, and the theoretical C3K stellar library (see Conroy & van Dokkum 2012). To fit the spectra, ALF α removes the continuum, by fitting a high-order Chebyshev polynomial to the ratio of the data to the model, and implements DYNESTY (Speagle 2020) or EMCEE (Foreman-Mackey et al. 2013) to sample the posteriors of 20 stellar population parameters. ALF and ALF α can fit spectra with wavelengths ranging from 3700 – 24000 Å and stellar populations older than 1 Gyr. For details, see Conroy &

offers simulated PSFs with one shutter, three adjacent shutters, or all shutters open. We test generating PSFs with three shutters open. Our resulting convolved R_e measurements are consistent with keeping all shutters open, and thus a simulated PSF with the same number of shutters open as the observations is not likely to impact our conclusions.

⁹ <https://github.com/alizabeverage/alfalpha>.

¹⁰ <https://github.com/cconroy20/alf/tree/master>.

¹¹ https://github.com/AlexaVillaume/SPI_Utils.

⁶ Interestingly, there are large differences between the spectra in some of the molecular bands between ~ 7000 –8000 Å. It is beyond the scope of this work to discuss these bands in detail. This will be the subject of future work.

⁷ <https://stpsf.readthedocs.io/en/latest/>.

⁸ Ideally, we would generate a PSF with the exact number of shutters open as in the SUSPENSE observations. However, STPSF currently only

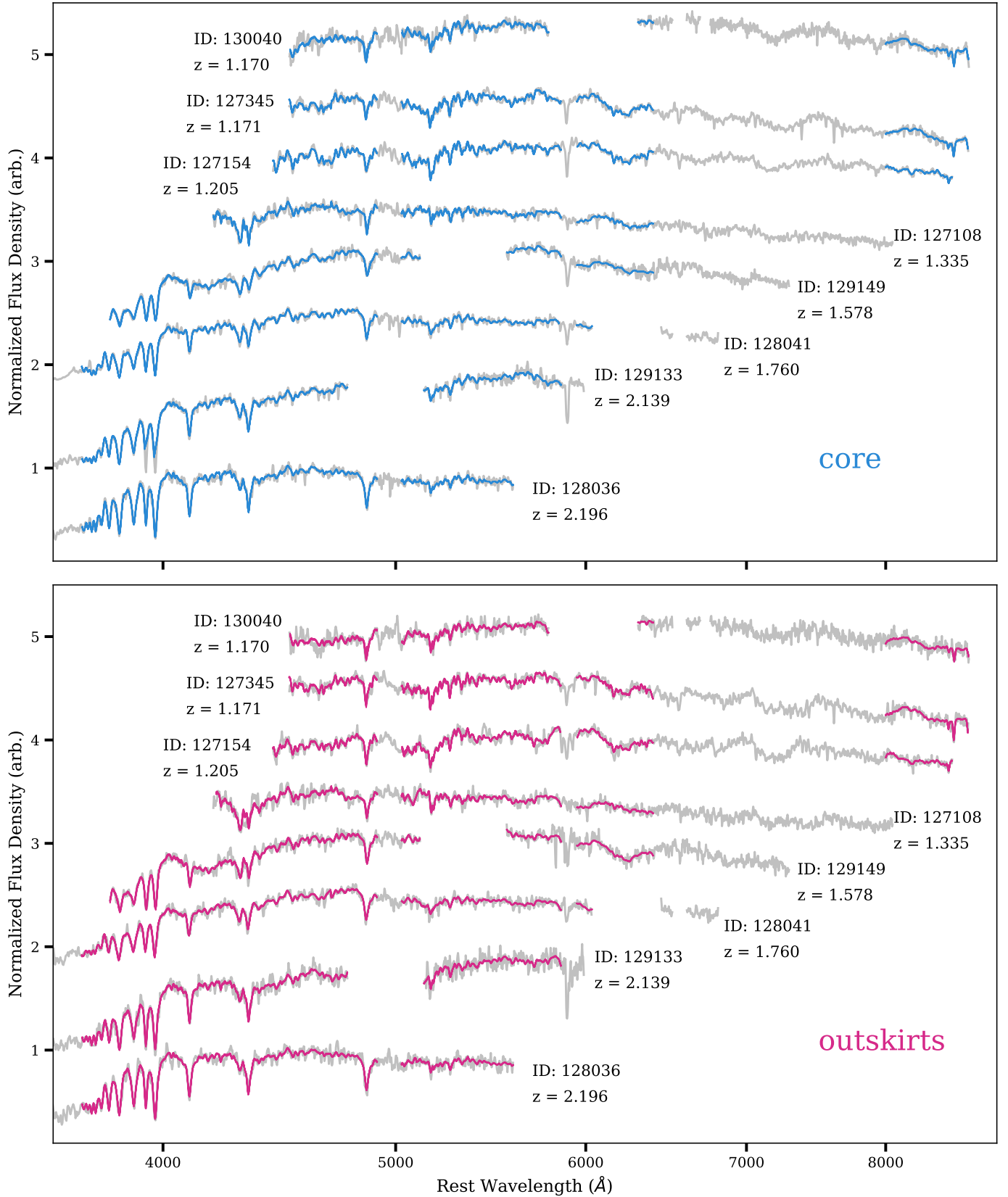


Fig. 3. Best-fitting ALFA models to our quiescent galaxy spectra. The core spectra (grey lines) are shown in the top panel in order of increasing redshift from top to bottom, with their best-fit models overplotted (blue lines). The outskirt spectra (grey lines) and fits (magenta lines) are similarly shown in the bottom panel. We normalise each spectrum by its median value between $4480 - 4520 \text{ \AA}$ and arbitrarily offset them in the y-direction for visibility. We do not show emission lines. This Figure serves to illustrate that many absorption lines are robustly detected for both the core and outskirt regions.

Table 2. The results from our $\text{ALF}\alpha$ fits to the spatially resolved SUSPENSE spectra.

ID	Radius (R_e)		log(Age/Gyr)		[Fe/H]		[Mg/Fe]		[Mg/H]	
	core	outskirt	core	outskirt	core	outskirt	core	outskirt	core	outskirt
130040	0.25	0.58	$0.50^{+0.19}_{-0.22}$	$0.43^{+0.22}_{-0.17}$	$-0.35^{+0.19}_{-0.23}$	$-0.41^{+0.20}_{-0.22}$	$-0.02^{+0.23}_{-0.17}$	$0.33^{+0.20}_{-0.22}$	$-0.37^{+0.23}_{-0.22}$	$-0.09^{+0.23}_{-0.27}$
127345	0.45	1.09	$0.54^{+0.15}_{-0.19}$	$0.35^{+0.10}_{-0.08}$	$-0.08^{+0.14}_{-0.17}$	$-0.07^{+0.12}_{-0.22}$	$0.21^{+0.12}_{-0.13}$	$0.33^{+0.15}_{-0.19}$	$0.13^{+0.16}_{-0.23}$	$0.25^{+0.15}_{-0.32}$
127154	0.74	1.66	$0.66^{+0.12}_{-0.17}$	$0.13^{+0.11}_{-0.09}$	$-0.06^{+0.09}_{-0.09}$	$0.14^{+0.15}_{-0.27}$	-	-	-	-
127108	0.59	1.12	$0.58^{+0.07}_{-0.13}$	$0.52^{+0.15}_{-0.14}$	$-0.55^{+0.14}_{-0.15}$	$-0.39^{+0.18}_{-0.22}$	$0.26^{+0.20}_{-0.20}$	$0.59^{+0.17}_{-0.23}$	$-0.29^{+0.19}_{-0.20}$	$0.20^{+0.16}_{-0.26}$
129149	1.5	3.21	$0.24^{+0.08}_{-0.05}$	$0.21^{+0.09}_{-0.08}$	$-0.12^{+0.12}_{-0.17}$	$-0.25^{+0.17}_{-0.23}$	$-0.20^{+0.27}_{-0.18}$	$-0.03^{+0.32}_{-0.26}$	$-0.34^{+0.23}_{-0.18}$	$-0.30^{+0.30}_{-0.27}$
128041	1.23	1.65	$0.14^{+0.07}_{-0.04}$	$0.09^{+0.10}_{-0.06}$	$-0.02^{+0.10}_{-0.16}$	$-0.08^{+0.14}_{-0.23}$	$0.10^{+0.16}_{-0.14}$	$0.13^{+0.22}_{-0.21}$	$0.06^{+0.15}_{-0.20}$	$0.03^{+0.22}_{-0.29}$
129133	0.77	1.92	$0.15^{+0.06}_{-0.05}$	$0.03^{+0.08}_{-0.06}$	$-0.20^{+0.16}_{-0.17}$	$-0.16^{+0.17}_{-0.29}$	-	-	-	-
128036	0.61	1.41	$0.09^{+0.04}_{-0.04}$	$0.00^{+0.07}_{-0.04}$	$-0.27^{+0.10}_{-0.22}$	$-0.27^{+0.17}_{-0.30}$	$0.18^{+0.17}_{-0.17}$	$0.30^{+0.21}_{-0.25}$	$-0.09^{+0.14}_{-0.24}$	$0.03^{+0.20}_{-0.36}$

van Dokkum (2012), Conroy et al. (2018), and Beverage et al. (2025). We note that $\text{ALF}\alpha$ has been thoroughly tested and shown to produce the same results as ALF (Beverage et al. 2025).

Prior to fitting, we smooth the $\text{ALF}\alpha$ models to the instrumental resolution of the NIRSpec-MSA observations, where we make use of the instrumental resolution derived via MSAFIT (de Graaff et al. 2024) by Slob et al. (2024). Slob et al. (2024) found that the wavelength dependence of the instrumental resolution is typically a factor of 1.3 better than pre-launch estimates from JDOx. We assume this corrected JDOx curve when fitting. See Slob et al. (2024) and Beverage et al. (2025) for details. We also mask the NaD absorption feature (which can be affected by the interstellar medium, Conroy & van Dokkum 2012), [OIII] lines, and H α +[NII] complex, where present, as in Beverage et al. (2025). Similar to Beverage et al. (2025), we exclude regions between 6400 - 8000 Å due to broad TiO absorption in the spectra. Thus, where possible, we fit the wavelength regions 3700 - 4700 Å, 4700 - 5100 Å, 5100 - 5800 Å, 5800 - 6400 Å, and 8000 - 8600 Å. Finally, in general, NIRSpec-MSA noise has been found to be underestimated (see, e.g., Maseda et al. 2023). Thus, we multiply our noise spectra by the jitter term (an average factor of 2.1) fit in Beverage et al. (2025) for each SUSPENSE galaxy, prior to fitting.

In our implementation of $\text{ALF}\alpha$, we use DYNESTY to sample the posteriors of the velocity offset, velocity dispersion, single SSP-equivalent stellar population age, isochrone metallicity, 10 elemental abundances (Fe, C, N, Mg, Na, Si, Ca, Ti, and Cr), Balmer emission line flux, emission line velocity and broadening, a shift in the T_{eff} of the fiducial isochrones, and an instrumental jitter term to account for over or underestimation of the observed uncertainties. We assume a Kroupa (2001) IMF. We set the upper limit of the age prior to be the age of the Universe at the redshift of each galaxy, plus 2 Gyr to allow for uncertainties. We assume the default priors for all other parameters. We examine the output ages and ensure that they are ≥ 1 Gyr, as $\text{ALF}\alpha$ is only suitable for stellar populations older than 1 Gyr.

We first fit the integrated spectrum, allowing for variation in all stellar parameters listed above. For the core and outskirt spectra, however, we cannot constrain all of the elemental abundances at this S/N (we determine this by fitting mock observations similar to Cheng et al. 2024). Thus, as in Cheng et al. (2024), we fix the values of all abundances other than Fe and Mg to the values from the integrated fits in our core and outskirt fits. In this way, we only allow age, Fe, and Mg to vary so that we can accurately constrain these parameters. We visually inspect the results for each individual galaxy to ensure that the posterior distributions for age, Fe, and Mg are well-sampled. If these posteriors run up against the priors, we extend the priors for [Z/H], [Fe/H], and [Mg/H] as needed by up to 0.2 dex. If

the re-fitted age, [Z/H], or [Fe/H], posteriors still run up against the priors, we discard these galaxies from our sample. For two galaxies (127154 and 129133), we find that the [Mg/H] posterior runs up against the extended prior in at least one of the three fits for these objects. Thus, for these objects only, we also fix the Mg abundance in the core and outskirt fits to the value recovered in the integrated fits, and do not report their Mg gradients. We also do not report the Mg gradient for 129149 as there are no detectable Mg features in the spectra of this galaxy. Finally, we find that the uncertainties on the age for dither 1 from 130040 are extremely large, so we discard this galaxy from our sample and only present the gradients from dither 2. We show our core and outskirt $\text{ALF}\alpha$ fits in Fig. 3.

We compare our integrated fit results with those of Beverage et al. (2025) for the 8 galaxies that we have in common (not shown). Our results are consistent within $\sim 0.2\sigma$, despite differences in the treatment of the data (i.e. the wiggle correction, see Section 3.1) and spectral extraction (see Slob et al. 2024).

4. Results

4.1. Spatially-resolved ages and elemental abundances

In Fig. 4, we show the ages and elemental abundances in the cores and outskirts of 8 massive, quiescent galaxies at $1.2 \leq z \leq 2.2$, derived by fitting the spectra with $\text{ALF}\alpha$. We show spatially resolved stellar population parameters as a function of de-projected radius from the centre of each galaxy. We report these values in Table 2. To estimate the uncertainties on the median values (stars), we perform a simple Monte Carlo simulation, where we take the median of the data points perturbed around the errors 1000 times, and show the 16th and 84th percentiles of this distribution in Fig. 4.

Fig. 4 indicates that massive, quiescent galaxies at $1.2 \leq z \leq 2.2$ from SUSPENSE tend to have negative age gradients, with galaxies having older cores compared to their outskirts, and positive [Mg/H] gradients, with galaxy cores being deficient in Mg compared to their outskirts. We also find positive [Mg/Fe] gradients, which may indicate that galaxy cores have longer SF timescales compared to galaxy outskirts (e.g., Matteucci 1994; Maiolino & Mannucci 2019). We discuss this further in Section 5.1. The individual SUSPENSE galaxies have diverse [Fe/H] gradients, although on average the [Fe/H] gradients are consistent with being flat, indicating that the cores and outskirts of these galaxies have similar metallicities. The fact that our fits prefer the galaxy cores to be older qualitatively agrees with the shallower H β feature that we see in the inset panel in Fig. 2. Similarly, the fact that we observe galaxy cores to have less Mg qualitatively agrees with the shallower Mgb feature. Ad-

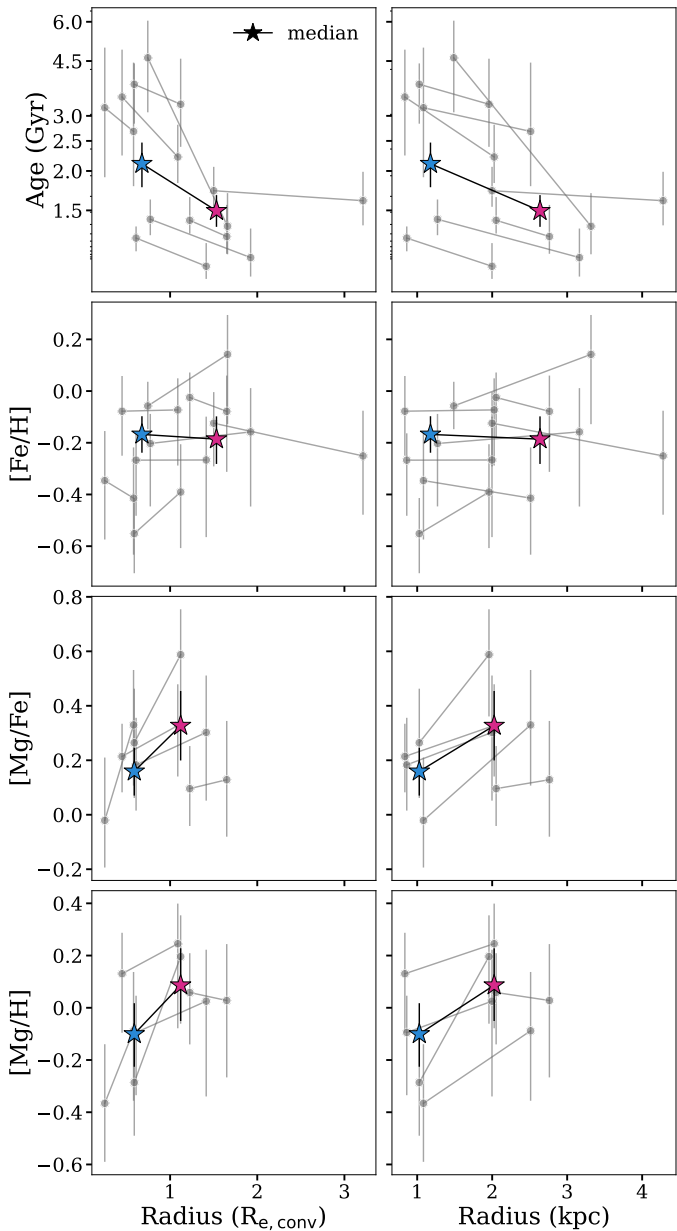


Fig. 4. Spatially-resolved stellar population parameters derived from our ALFA full spectrum fits. In the left column, we plot our measured parameters as a function of de-projected radius in units of R_e (determined as described in Section 3.3). In the right column, we plot our measured parameters as a function of de-projected radius in units of kpc. We show age in the top row, [Fe/H] in the second row, [Mg/Fe] in the third row, and [Mg/H] in the bottom row. In each panel, we show the measured parameters for each individual galaxy as points connected by lines. We show the median parameters as stars connected by lines.

ditionally, the contrasting differences in the core and outskirt spectra that we see in the Fe52 and Fe53 features could be contributing to our observed flat [Fe/H] gradient. We discuss the implications of these results for galaxy formation and assembly in Sections 5.1 and 5.2.

It is interesting to note that our results differ from gradients measured at lower z . In particular, massive, quiescent galaxies typically have flat age and [Mg/Fe] gradients, and negative metallicity gradients out to $z \sim 1$ (e.g., [Mehlert et al. 2003](#); [Greene et al. 2015](#); [Martín-Navarro et al. 2018](#); [Cheng et al. 2024](#); [Parikh et al. 2024](#)). This suggests that stellar population

gradients in massive, quiescent galaxies may evolve from what we find at $1.2 \lesssim z \lesssim 2.2$ to what has been found at $z \lesssim 1$. In this context, it is interesting to note that the smallest quiescent galaxies in the local Universe (i.e., relic galaxies), have been found to have positive [Mg/Fe] gradients ([Martín-Navarro et al. 2018](#)), qualitatively similar to what we see here. We discuss this further in Section 5.

There are also a handful of other studies that have measured spatially-resolved spectroscopic stellar population gradients in massive quiescent galaxies beyond $z \sim 1$. Specifically, [Jafariyazani et al. \(2020\)](#) measured a flat age and [Mg/Fe] gradient, and a negative [Fe/H] gradient in a massive lensed galaxy at $z = 1.98$, which is qualitatively consistent with results at $z \lesssim 1$. [Akhshik et al. \(2023\)](#) found diverse age gradients in 8 lensed galaxies at $1.6 < z < 2.9$. [Ditrani et al. \(2022\)](#) measured age and metal gradients in 4 galaxies at $1.6 < z < 2.4$ and found flat age and negative metallicity gradients, again consistent with results at $z \lesssim 1$. Finally, [Pérez-González et al. \(2024\)](#) found a strong negative total metallicity gradient in an individual galaxy at $z \sim 3.7$ and [D'Eugenio et al. \(2024\)](#) measured a constant age as a function of radius in an individual galaxy at $z \sim 3$. It is not surprising that different works find diverse gradients beyond $z \sim 1$ as different methods are used in each of these studies. Additionally, the sample sizes for which stellar population gradients can be measured at these redshifts (both in our work and in previous studies) are very small. Finally, previous work examined relatively younger quiescent galaxies, which could explain some of these differences. We discuss this further in Section 4.2.

4.2. Trends between gradients and galaxy parameters

As we have age and [Fe/H] gradients for our whole sample, we examine if there are any correlations with global velocity dispersions, integrated ages, and spatially-resolved stellar kinematics. These parameters are commonly used as measures of evolutionary stage. In Fig. 5, we show the gradient slopes as a function of different galaxy parameters. We fit a line to the points in each panel using the non-linear least squares algorithm implemented in the `scipy curve_fit` function, in the `optimize` module ([Virtanen et al. 2020](#)). We compute the Pearson- r correlation coefficient and corresponding p -value, which we state in each panel.

In the left column, there is a mild positive trend between age gradients and velocity dispersion and a strong negative correlation with [Fe/H] gradients, although note that both trends are statistically insignificant. Thus, galaxies with higher velocity dispersions may have flatter age gradients and more negative [Fe/H] gradients. The tentative trends that we see with age and [Fe/H] are in contrast with results at low- z from [Sánchez-Blázquez et al. \(2007\)](#), [Kuntschner et al. \(2010\)](#), [Spolaor et al. \(2010\)](#), [Pastorello et al. \(2014\)](#), [González Delgado et al. \(2015\)](#), [Greene et al. \(2015\)](#), [Martín-Navarro et al. \(2018\)](#), and [Santucci et al. \(2020\)](#). On the other hand, [Ferreras et al. \(2019\)](#) found a positive trend between total metallicity gradients and σ in a large sample of local early-type galaxies, consistent with our findings.

In the middle column of Fig. 5, there is a mild negative trend between age gradients and age and mild positive trend between [Fe/H] gradients and age, although these trends are also insignificant. Thus, younger quiescent galaxies may have flatter age gradients and more negative [Fe/H] gradients, while older quiescent galaxies may have more negative age gradients and more positive [Fe/H] gradients. Interestingly, these tentative trends are qualitatively similar to the results of [Cheng et al. \(2024\)](#), who found a negative trend between age gradients and age and a positive trend between [Fe/H] gradients and age in quiescent galaxies

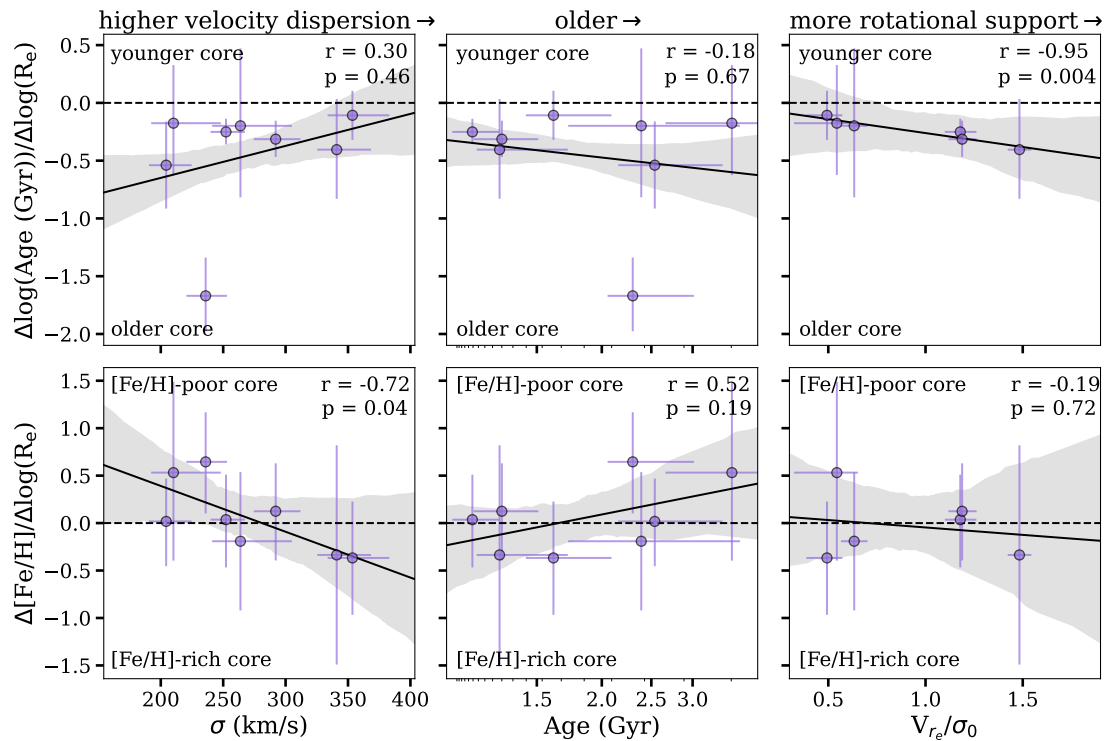


Fig. 5. Spatially resolved age and [Fe/H] gradients, normalized by R_e (see Section 3.3), as a function of galaxy parameters. We show the age gradients in the top row and the [Fe/H] gradients in the bottom row. The outlying object with a strongly negative age gradient is 127154. We show the integrated velocity dispersion (σ , from our ALFα fits to the integrated spectra) in the left column, the integrated age (from our integrated ALFα fits) in the middle, and V_{r_e}/σ_0 (measured in Slob et al. 2025) on the right. Horizontal dashed lines indicate where flat gradients would lie. We perform a linear fit to the points in each panel, shown by the solid lines, with 1σ bootstrapped uncertainties indicated by the shaded regions.

at $0.6 \lesssim z \lesssim 1.0$. However, we note that while our age gradients may evolve from flat to negative with increasing age, the gradients in Cheng et al. (2024) evolved from positive to flat (although we sample a slightly younger age range).

In this context, the tentative trends that we find between stellar population gradients and age may be qualitatively consistent with previous spatially-resolved studies at $z > 1$. In particular, Jafariyazani et al. (2020), Pérez-González et al. (2024), and D’Eugenio et al. (2020) all examine relatively young galaxies and find flat/slightly negative age gradients and negative metallicity gradients. This is also what we may be seeing at the youngest end of the age axis in the middle column of Fig. 5.

Finally, in the right column of Fig. 5, we compare our gradients to spatially resolved stellar kinematics measured in Slob et al. (2025). In particular, Slob et al. (2025) derived their kinematic measurements from the NIRSpec-MSA spectra using a forward modelling approach. We show our stellar population gradients as a function of their V_{r_e}/σ_0 , where a higher value of V_{r_e}/σ_0 indicates more rotational support. We find a significant negative correlation between our age gradients and V_{r_e}/σ_0 , and a mild negative correlation between our [Fe/H] gradients and V_{r_e}/σ_0 (which is insignificant). Thus, galaxies with more rotational support may have more strongly negative age and [Fe/H] gradients. On the other hand, Greene et al. (2019) found no significant correlations between stellar population gradients and the ratio of rotational to dispersion support in massive, local, elliptical galaxies. We discuss our trends in Sections 5.1 and 5.2.

5. Discussion

5.1. Inside-out quenching

Despite its central role in galaxy formation and evolution, galaxy quenching is still not well understood. There are a variety of proposed mechanisms, both internal (e.g., Di Matteo et al. 2005; Bower et al. 2006; Croton et al. 2006; Martig et al. 2009) and environmental (e.g., Dekel & Birnboim 2006; van den Bosch et al. 2008; Wetzel et al. 2012). As our galaxies are observed early, in the peak of the quenching era ($z \sim 1 - 3$, e.g., Whitaker et al. 2012), and are therefore relatively unpolluted by potential late-time mergers compared to nearby quiescent galaxies, their gradients may provide interesting clues to the quenching process.

The negative age gradients that we find may be the imprint of inside-out growth and quenching, where star formation first occurs and/or terminates in the central regions of galaxies, followed by later-time star formation and/or quenching in the outskirts (e.g., Dekel & Burkert 2014; Tacchella et al. 2015b,a, 2016, 2018; Zolotov et al. 2015, see also Zibetti et al. 2020, who came to a similar conclusion). Our work is therefore consistent with studies of massive star-forming galaxies (i.e., the possible progenitors of the quiescent galaxies in our sample), which find higher specific star-formation rates (sSFRs) in galaxy outskirts and lower sSFRs or quenched star formation in galaxy cores (e.g. Barro et al. 2013, 2017; Nelson et al. 2016, 2021; Spilker et al. 2019; Tacchella et al. 2018).

While our age gradients point to inside-out quenching, our [Mg/Fe] gradients suggest that the star-formation timescale in the core is longer than in the outskirts (see, e.g., Matteucci 1994; Maiolino & Mannucci 2019). This is not what we expect from inside-out quenching, in the case that both populations started

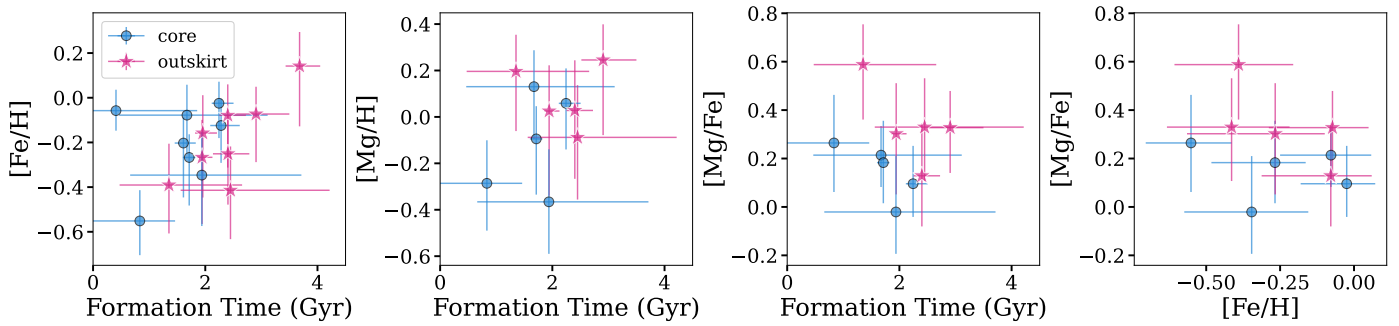


Fig. 6. Individual core and outskirt elemental abundances. In the first three panels, we show formation time on the x -axis, which we compute by correcting the stellar age (from our ALFA fits to the integrated spectra) by the age of the Universe at the redshift of each galaxy. We show our $[\text{Fe}/\text{H}]$ abundances in the first panel, $[\text{Mg}/\text{H}]$ abundances in the second panel, and $[\text{Mg}/\text{Fe}]$ abundances in the third panel. In the fourth panel, we show $[\text{Mg}/\text{Fe}]$ as a function of $[\text{Fe}/\text{H}]$. In each panel, core values are shown as points and outskirt values are shown as stars.

forming at the same time. However, it is possible that star formation in the outskirts also started much later and occurred over a shorter time compared to the core. In this scenario, the core would have formed earlier than the outskirts, with the entire galaxy quenching simultaneously.

On the other hand, it is also important to note that our measurements are luminosity-weighted, and thus our ages and $[\text{Mg}/\text{Fe}]$ ratios, which may be driven by different wavelengths, may reflect slightly different stellar populations (although this effect may be minor). Moreover, $[\text{Mg}/\text{Fe}]$ is also influenced by the star-formation efficiency, the IMF, and outflows (see, e.g., Tinsley 1979; Zolotov et al. 2010; Martín-Navarro 2016; Andrews et al. 2017; Sybilska et al. 2018). In this study, our $[\text{Mg}/\text{Fe}]$ gradients are driven more by $[\text{Mg}/\text{H}]$ than $[\text{Fe}/\text{H}]$, as we find flat $[\text{Fe}/\text{H}]$ gradients but positive $[\text{Mg}/\text{H}]$ gradients (see Fig. 4).

Our $[\text{Mg}/\text{H}]$ gradients in turn may be regulated by whether and how quickly the gas supply in the centres of the galaxies was depleted during the quenching process (see, e.g., Ellison et al. 2018; Spilker et al. 2019; Trussler et al. 2020; Beverage et al. 2021). Specifically, a lower $[\text{Mg}/\text{H}]$ abundance will result if the gas supply is removed before it can enrich (see also Beverage et al. 2025). In particular, Beverage et al. (2021) compared different chemical evolution models from Spitoni et al. (2017) and found that abrupt gas expulsion prevents the galaxy from further enriching, leading to lower metallicities for stellar populations that quench earlier, in agreement with observations (e.g., Kriek et al. 2016; Kriek et al. 2019; Jafariyazani et al. 2025; Beverage et al. 2023, 2024, 2025; Carnall et al. 2022; Zhuang et al. 2023). This scenario can thus explain our observed $[\text{Mg}/\text{H}]$ abundances if the cores quenched more abruptly (perhaps due to AGN outflows, e.g., Croton et al. 2006; Bluck et al. 2014; Zolotov et al. 2015; Tacchella et al. 2015a, 2016; Belli et al. 2024; Park et al. 2024), while the outskirts continued to form stars.

The inside-out quenching scenario presented here is reinforced by Fig. 6, where we examine the general core and outskirt stellar populations in SUSPENSE as a function of formation time. First, similar to Beverage et al. (2025), we find that earlier-forming stellar populations have slightly lower $[\text{Fe}/\text{H}]$ and $[\text{Mg}/\text{H}]$. Moreover, galaxy cores overall formed earlier than galaxy outskirts and are less enriched by the time they stop forming stars. Thus, this Figure reinforces the idea that the cores of the SUSPENSE galaxies formed faster and quenched more efficiently at earlier times.

Although the scenario above can explain the $[\text{Mg}/\text{H}]$ and age gradients, it is puzzling that we find flat $[\text{Fe}/\text{H}]$ gradients, as we would also expect more iron-deficient cores in this scenario.

Thus, additional factors like late-time mergers (discussed in Section 5.2) and IMF gradients (see Section 5.3) may be needed to explain all trends. Furthermore, our sample is small, and larger samples are required to come to definitive conclusions.

Finally, we note that our results are inconsistent with a scenario in which galaxies quench their star formation via wet, gas-rich major mergers. Major mergers are expected to result in outside-in quenching, by funneling gas to the galaxy's centre and triggering a central starburst. This would result in a positive age gradient (Hopkins et al. 2008; Snyder et al. 2011; Wellons et al. 2015; Pathak et al. 2021), which is generally inconsistent with our findings. Nonetheless, it is possible that different quenching mechanisms operate at different redshifts. For example, Cheng et al. (2024) find positive age gradients in their youngest massive, quiescent galaxies at $0.6 \lesssim z \lesssim 1.0$, consistent with central starbursts triggered by wet mergers.

5.2. Galaxy growth via minor mergers

Below $z \sim 1$, resolved studies have revealed that massive, quiescent galaxies tend to have flat age and α -element abundance gradients and negative metallicity gradients (e.g., Mehrt et al. 2003; Greene et al. 2015; Martín-Navarro et al. 2018; Cheng et al. 2024). These findings are consistent with inside-out growth, where outskirts are built up by the accretion of low-mass, low-metallicity satellites (minor mergers, e.g., Bezanson et al. 2009; Naab et al. 2009; van de Sande et al. 2013). Alternatively, the observed evolution in galaxy properties over cosmic time can be due to progenitor bias. In this scenario, where the quiescent population grows by the addition of larger galaxies at later times (van Dokkum & Franx 2001; Carollo et al. 2013; Poggianti et al. 2013), gradients may come directly from the star-forming progenitors (Cheng et al. 2024, see Jones et al. 2015; Tripodi et al. 2024; Shen et al. 2024; Ju et al. 2025), or could be produced by the quenching mechanism (see Section 5.1).

Here, we measure resolved stellar population gradients out to $z \sim 2.2$, targeting the peak era of quenching and assembly activity (Oser et al. 2010; Rodriguez-Gomez et al. 2016; Whitaker et al. 2012). Assuming that the SUSPENSE galaxies are representative of the progenitors of $z \lesssim 1$ massive, quiescent galaxies, it is interesting to compare our results with those from lower redshift studies. In contrast to the flat age gradients at $z \lesssim 1$, we find negative age gradients at $1.2 \lesssim z \lesssim 2.2$. In addition, while negative $[\text{Fe}/\text{H}]$ gradients are found at lower redshifts, we find flat $[\text{Fe}/\text{H}]$ gradients. Finally, we find positive $[\text{Mg}/\text{Fe}]$ gradients, in contrast with the flat $[\text{Mg}/\text{Fe}]$ gradients at $z \lesssim 1$. Thus, age gra-

dients may evolve from negative to flat, $[\text{Fe}/\text{H}]$ gradients may evolve from flat to negative, and $[\text{Mg}/\text{Fe}]$ gradients may evolve from positive to flat between $z \sim 2$ and $z \sim 1$. This evolution could be due to inside-out growth via minor mergers, if the accreted galaxies are older and have lower $[\text{Fe}/\text{H}]$ and $[\text{Mg}/\text{Fe}]$. In this scenario, the stars of these satellite galaxies will primarily be deposited in the outskirts, and may flatten the age and $[\text{Mg}/\text{H}]$ gradients that were generated by inside-out quenching, while simultaneously steepening the $[\text{Fe}/\text{H}]$ gradients in the negative direction (see also [Zibetti et al. 2020](#)).

This minor merger picture may be supported by some of the trends that we see with galaxy properties in Fig. 5. In particular, in the right column, we compare our resolved stellar population gradients to the 6 galaxies that we have in common with [Slob et al. \(2025\)](#), who measured spatially resolved stellar kinematics in 15 SUSPENSE galaxies. Interestingly, we find a significant negative trend between our age gradients and V_{r_e}/σ_0 , where galaxies with more rotational support also have stronger negative age gradients. This supports the scenario presented in [Slob et al. \(2025\)](#), where minor mergers gradually destroy rotational support over time while simultaneously flattening the age gradients (again, assuming that the accreted galaxies are older). However, larger sample sizes are required to constrain the trends between $[\text{Fe}/\text{H}]$ gradients and V_{r_e}/σ_0 , and between age and $[\text{Fe}/\text{H}]$ gradients and galaxy age, to assess whether these are also consistent with this picture (see also [D'Eugenio et al. 2024](#)).

Alternatively, progenitor bias is also expected to produce age and metal gradients ([Larson 1974](#); [White 1980](#); [Kobayashi 2004](#); [Pipino et al. 2008, 2010](#)). In this case, galaxies evolve passively after quenching. The different gradients could indicate that different quenching processes operate at different times, as we suggest in Section 5.1.

If progenitor bias is playing a significant role and these galaxies are not affected by minor mergers, then some of these high- z galaxies must survive as they are until the present day. Relic galaxies may represent this unique subpopulation, in which the early-forming cores of massive, quiescent galaxies have passively evolved since $z \sim 2$ without accreting *ex situ* material ([Trujillo et al. 2009](#); [Quilis & Trujillo 2013](#); [Stringer et al. 2015](#)). Thus, in the progenitor bias scenario, they may represent the descendants of distant quiescent galaxies like those in SUSPENSE. Interestingly, similar to our findings, [Martín-Navarro et al. \(2018\)](#) found positive $[\text{Mg}/\text{Fe}]$ gradients and flat age and metallicity gradients in a sample of nearby relic galaxies. On the other hand, our age and metallicity gradients are inconsistent with the results of [Martín-Navarro et al. \(2018\)](#). The qualitatively similar $[\text{Mg}/\text{Fe}]$ gradients could be indicative of the progenitor bias picture, with galaxies maintaining their $[\text{Mg}/\text{Fe}]$ gradients until the present day. Of course, it is also possible that both mechanisms (i.e. progenitor bias and minor mergers) are playing a role (e.g., [van der Wel et al. 2008](#); [Hopkins et al. 2010](#); [Oser et al. 2012](#); [Newman et al. 2012](#)).

5.3. Caveats

In this work, we presented age and elemental abundance gradients in 8 massive, quiescent galaxies at $1.2 \lesssim z \lesssim 2.2$. We emphasize that this is the first study of its kind, with the largest sample size to date. Thus, we have demonstrated that it is possible to measure stellar population gradients in galaxies beyond $z \sim 1$ using the *JWST*/NIRSpec-MSA. However, there are some caveats that should be taken into consideration.

There are a few observational factors affecting our data, including the limited spatial resolution and convolved nature of the

MSA spectra, and the fact that the arbitrary position of the micro shutters does not always allow us to capture each galaxy's precise centre. Despite our efforts to determine the exact regions of the galaxies contained within each micro shutter (see Section 3.3), these factors likely result in some contamination from the outskirts in our core spectra and vice versa. However, any contamination is likely minor, as we detect gradients in our galaxies. This detection suggests that our measured gradients are real, as contamination from different regions of the galaxy will serve to weaken gradients (see [Cheng et al. 2024](#)). High spatial resolution follow-up with current or planned IFU instruments (i.e. the NIRSpec-IFU, ERIS on the VLT, HARMONI on the ELT) may provide a more detailed view of assembly histories by allowing measurements of detailed stellar population profiles (see, e.g., [Oyarzún et al. 2019](#)) and avoiding MSA slitlet offsets.

Our fitting technique could also be biasing our results, as we only rely on one code (*ALFA*). Nonetheless, the stacked spectra that we show in Fig. 2 demonstrate that the data require negative age and positive $[\text{Mg}/\text{H}]$ gradients, with a shallower core $\text{H}\beta$ feature indicating an older age and a shallower $\text{Mg}\beta$ feature indicating less $[\text{Mg}/\text{H}]$. Additionally, the fact that the Fe52 and Fe53 features show opposing core and outskirt depths indicates that the data also require a flat $[\text{Fe}/\text{H}]$ gradient. Thus, while the absolute values of our elemental abundances could be affected by our fitting technique, our qualitative gradients and our conclusions about them are presumably robust.

It is also possible that the IMF could be contributing to the $[\text{Mg}/\text{Fe}]$ gradient as elemental abundances and abundance ratios are dependent on the IMF (e.g., [Martín-Navarro 2016](#); [Martín-Navarro et al. 2018](#); [De Lucia et al. 2017](#); [Fontanot et al. 2017](#)). In this work, we assume a [Kroupa \(2001\)](#) IMF, but there are indications that the low-mass end (e.g., [van Dokkum et al. 2017](#); [Gu et al. 2022](#)) and perhaps also the high-mass end (e.g., [Fontanot et al. 2017](#), see also [van Dokkum & Conroy 2024](#)) of the IMF in the SUSPENSE galaxies may deviate from the [Kroupa \(2001\)](#) form (see also [Slob et al. 2025](#)). In particular, a variable IMF can affect the ratio of Mg to Fe by changing the relative number of core-collapse supernovae (which primarily produce Mg) compared to Type Ia supernovae (which primarily produce Fe, [Matteucci 1994](#); [Thomas et al. 1999](#)). In general, it is very challenging to constrain the shape of the IMF, as well as its impact on elemental abundances. In the future, a robust characterization of the slope of the IMF in distant quiescent galaxies, as well as detailed chemical evolution modeling to understand the effects of both star-formation timescales and the IMF on elemental abundance patterns, are required (see also [Beverage et al. 2025](#)).

Finally, while this is the largest sample of $z \gtrsim 1$ galaxies for which gradients have been derived using this method so far, our sample size is still small, which makes it challenging to draw strong conclusions about the population of galaxies at these redshifts. Thus, in the future, it will be informative to make the same measurements in a statistically significant sample of galaxies, perhaps with similar follow-up NIRSpec-MSA observations.

6. Summary and conclusions

Spatially resolving the stellar populations of massive, quiescent galaxies at early times can reveal crucial information about how galaxies quenched their star formation and assembled their stellar populations. Previous work beyond the local Universe has been based on photometry or very small spectroscopic sample sizes. In this work, we leveraged the capabilities of the *JWST*/NIRSpec-MSA and presented age, $[\text{Fe}/\text{H}]$, $[\text{Mg}/\text{H}]$, and $[\text{Mg}/\text{Fe}]$ gradients in 8 massive, quiescent galaxies at $1.2 \lesssim z \lesssim 2.2$.

2.2 from *JWST*-SUSPENSE, an ultra-deep spectroscopic survey (Slob et al. 2024). These gradients were derived by fitting the core and outskirt spectra of each galaxy with ALFA, a flexible, full-spectrum SPS model (Conroy & van Dokkum 2012; Conroy et al. 2018; Beverage et al. 2024, 2025). Our study accounts for the fact that the NIRSpec-MSA micro shutters are not centred or aligned on the galaxies in our sample, as well as for spatial undersampling of the *JWST* PSF. In summary, we found:

- Massive, quiescent galaxies at $1.2 \lesssim z \lesssim 2.2$ from SUSPENSE tend to have negative age gradients, positive [Mg/H] and [Mg/Fe] gradients, and flat [Fe/H] gradients. In other words, the cores of the SUSPENSE galaxies are older, Mg-enhanced, and have approximately the same [Fe/H] compared to their outskirts.
- The negative age gradients suggest inside-out quenching (e.g., Tacchella et al. 2016, 2018), where star formation terminated early in galaxy cores, while galaxy outskirts continued to form stars until later times. The low central [Mg/H] may indicate rapid central gas expulsion (e.g., Beverage et al. 2021, 2025), further supporting the inside-out quenching scenario. Thus, galaxy cores formed earlier and stopped their star formation more abruptly, preventing further enrichment. Meanwhile, galaxy outskirts formed later and experienced more enrichment before quenching. It is unclear how our flat [Fe/H] and positive [Mg/Fe] gradients fit into this picture.
- Our gradients differ from those at lower- z , where studies typically find flat age and [Mg/Fe] gradients and negative [Fe/H] gradients (e.g., Greene et al. 2015; Martín-Navarro et al. 2018; Cheng et al. 2024). Thus, gradients may evolve over cosmic time.
- We found marginal correlations between our gradients and galaxy properties including global velocity dispersion, integrated galaxy age, and V_r/σ_0 . In particular, we found that age gradients are stronger in galaxies that have more rotational support. This trend, and the fact that gradients may evolve over time, suggest that galaxy growth may continue post-quenching via minor mergers (e.g., Bezanson et al. 2009; Naab et al. 2009; van de Sande et al. 2013). In this case, the accretion of old, low-mass, low-metallicity, and low-[Mg/Fe] satellites could act to flatten age and [Mg/Fe] gradients and build up negative [Fe/H] gradients, while simultaneously increasing galaxy sizes (e.g., Trujillo et al. 2004; van Dokkum et al. 2010; van der Wel et al. 2014) and decreasing their rotational support (Slob et al. 2025).
- The observed "evolution" in gradients may also be explained by different quenching mechanisms occurring at different times, with early-time quenching generating the negative age and flat [Fe/H] gradients that we found, and late-time quenching resulting in the negative [Fe/H] and flat age gradients found at lower z . Interestingly, the positive [Mg/Fe] gradients that we measured were also found in nearby relic galaxies (Martín-Navarro et al. 2018). These may be the "unpolluted" descendants of our galaxies, in which little-to-no late-time merger activity occurred. In reality, both late-time mergers and different quenching mechanisms may be playing a role (e.g., Oser et al. 2012; Newman et al. 2012).

In this work, we have probed the peak of the star-formation quenching and galaxy assembly era, with the first detailed stellar population gradients derived in a sample of distant massive, quiescent galaxies using ultra-deep *JWST*/NIRSpec-MSA spectra. This study has allowed us to drive closer to the detailed formation histories of such galaxies, suggesting that their cores formed

earlier and quenched more abruptly than their outskirts. However, there are still a number of open questions. For example, it is not clear why we find a positive [Mg/H] gradient, but no gradient in [Fe/H]. It is also unclear how the IMF behaves in these galaxies, and how it may affect the derived stellar population gradients. In the future, larger sample sizes, increased spatial resolution, and a robust characterization of the stellar IMF will paint an even clearer picture of the physical processes at play in the evolution of these galaxies.

Acknowledgements. We thank Antoine Dumont, Ciarán Rogers, and Colin Yip for useful conversations. We thank the *JWST*/NIRSpec helpdesk for their support. This work is based on observations made with the NASA/ESA/CSA *JWST*. The data were obtained from the Mikulski Archive for Space Telescopes (MAST) at the Space Telescope Science Institute (STScI), which is operated by the Association of Universities for Research in Astronomy, Inc., under NASA contract NAS 5-03127 for *JWST*. These observations are associated with program *JWST*-GO-2110. Support for program *JWST*-GO-2110 was provided by NASA through a grant from the STScI. Some of the data products presented herein were retrieved from the Dawn *JWST* Archive (DJA). DJA is an initiative of the Cosmic Dawn Center (DAWN), which is funded by the Danish National Research Foundation under grant DNRF140. This work was performed using the compute resources from the Academic Leiden Interdisciplinary Cluster Environment (ALICE) provided by Leiden University. This work also used the Dutch national e-infrastructure with the support of the SURF Cooperative using grant no. EINF-10017 which is financed by the Dutch Research Council (NWO). MK acknowledges funding from the NWO through the award of the Vici grant VI.C.222.047 (project 2010007169).

References

- Akhshik, M., Whitaker, K. E., Leja, J., et al. 2023, ApJ, 943, 179
 Anderson, J. 2016, Empirical Models for the WFC3/IR PSF, Instrument Science Report WFC3 2016-12, 42 pages
 Andrews, B. H., Weinberg, D. H., Schönrich, R., & Johnson, J. A. 2017, ApJ, 835, 224
 Astropy Collaboration, Price-Whelan, A. M., Lim, P. L., et al. 2022, ApJ, 935, 167
 Barro, G., Faber, S. M., Koo, D. C., et al. 2017, ApJ, 840, 47
 Barro, G., Faber, S. M., Pérez-González, P. G., et al. 2013, ApJ, 765, 104
 Bell, E. F. & de Jong, R. S. 2001, ApJ, 550, 212
 Belli, S., Park, M., Davies, R. L., et al. 2024, Nature, 630, 54
 Beverage, A. 2024, alizabeverage/alfalpha: Initial Release alongside Beverage et al. 2024
 Beverage, A. G., Kriek, M., Conroy, C., et al. 2021, ApJ, 917, L1
 Beverage, A. G., Kriek, M., Conroy, C., et al. 2023, ApJ, 948, 140
 Beverage, A. G., Kriek, M., Suess, K. A., et al. 2024, ApJ, 966, 234
 Beverage, A. G., Slob, M., Kriek, M., et al. 2025, ApJ, 979, 249
 Bezanson, R., van Dokkum, P. G., Tal, T., et al. 2009, ApJ, 697, 1290
 Bluck, A. F. L., Mendel, J. T., Ellison, S. L., et al. 2014, MNRAS, 441, 599
 Bower, R. G., Benson, A. J., Malbon, R., et al. 2006, MNRAS, 370, 645
 Bradley, L., Sipócz, B., Robitaille, T., et al. 2024, astropy/photutils: 1.12.0
 Brammer, G. 2023, grizli
 Bruzual, G. & Charlot, S. 2003, MNRAS, 344, 1000
 Bushouse, H., Eisenhamer, J., Dencheva, N., et al. 2023, JWST Calibration Pipeline
 Carnall, A. C. 2017, arXiv e-prints, arXiv:1705.05165
 Carnall, A. C., McLure, R. J., Dunlop, J. S., et al. 2022, ApJ, 929, 131
 Carollo, C. M., Bschott, T. J., Renzini, A., et al. 2013, ApJ, 773, 112
 Casey, C. M., Kartaltepe, J. S., Drakos, N. E., et al. 2023, ApJ, 954, 31
 Cheng, C. M., Kriek, M., Beverage, A. G., et al. 2024, MNRAS, 532, 3604
 Choi, J., Dotter, A., Conroy, C., et al. 2016, ApJ, 823, 102
 Ciocca, F., Saracco, P., Gargiulo, A., & De Propris, R. 2017, MNRAS, 466, 4492
 Conroy, C. & van Dokkum, P. 2012, ApJ, 747, 69
 Conroy, C., Villaume, A., van Dokkum, P. G., & Lind, K. 2018, ApJ, 854, 139
 Croton, D. J., Springel, V., White, S. D. M., et al. 2006, MNRAS, 365, 11
 Damjanov, I., Sohn, J., Geller, M. J., Utsumi, Y., & Dell'Antonio, I. 2023, ApJ, 943, 149
 Damjanov, I., Zahid, H. J., Geller, M. J., et al. 2019, ApJ, 872, 91
 de Graaff, A., Rix, H.-W., Carniani, S., et al. 2024, A&A, 684, A87
 De Lucia, G., Fontanot, F., & Hirschmann, M. 2017, MNRAS, 466, L88
 Dekel, A. & Birnboim, Y. 2006, MNRAS, 368, 2
 Dekel, A. & Burkert, A. 2014, MNRAS, 438, 1870
 D'Eugenio, F., Pérez-González, P. G., Maiolino, R., et al. 2024, Nature Astronomy, 8, 1443
 D'Eugenio, F., van der Wel, A., Wu, P.-F., et al. 2020, MNRAS, 497, 389

- Di Matteo, T., Springel, V., & Hernquist, L. 2005, *Nature*, 433, 604
- Dittrani, F. R., Andreon, S., Longhetti, M., & Newman, A. 2022, *A&A*, 660, A132
- Dressel, L., Hodge, P., & Barrett, P. 2007, *wx2d: A PyRAF Routine to Resample Spectral Images*, Instrument Science Report STIS 2007-04, 20 pages
- Dumont, A., Neumayer, N., Seth, A. C., et al. 2025, arXiv e-prints, arXiv:2503.09697
- Ellison, S. L., Sánchez, S. F., Ibarra-Medel, H., et al. 2018, *MNRAS*, 474, 2039
- Ferreras, I., Scott, N., La Barbera, F., et al. 2019, *MNRAS*, 489, 608
- Ferruit, P., Jakobsen, P., Giardino, G., et al. 2022, *A&A*, 661, A81
- Fontanot, F., De Lucia, G., Hirschmann, M., et al. 2017, *MNRAS*, 464, 3812
- Foreman-Mackey, D., Hogg, D. W., Lang, D., & Goodman, J. 2013, *PASP*, 125, 306
- Franx, M. & Illingworth, G. 1990, *ApJ*, 359, L41
- Franx, M., van Dokkum, P. G., Förster Schreiber, N. M., et al. 2008, *ApJ*, 688, 770
- Gallazzi, A., Charlot, S., Brinchmann, J., White, S. D. M., & Tremonti, C. A. 2005, *MNRAS*, 362, 41
- Goddard, D., Thomas, D., Maraston, C., et al. 2017, *MNRAS*, 465, 688
- González Delgado, R. M., García-Benito, R., Pérez, E., et al. 2015, *A&A*, 581, A103
- Greene, J. E., Janish, R., Ma, C.-P., et al. 2015, *ApJ*, 807, 11
- Greene, J. E., Murphy, J. D., Graves, G. J., et al. 2013, *ApJ*, 776, 64
- Greene, J. E., Veale, M., Ma, C.-P., et al. 2019, *ApJ*, 874, 66
- Griffith, R. L., Cooper, M. C., Newman, J. A., et al. 2012, *ApJS*, 200, 9
- Gu, M., Greene, J. E., Newman, A. B., et al. 2022, *ApJ*, 932, 103
- Hopkins, P. F., Cox, T. J., Dutta, S. N., et al. 2009, *ApJS*, 181, 135
- Hopkins, P. F., Cox, T. J., Kereš, D., & Hernquist, L. 2008, *ApJS*, 175, 390
- Hopkins, P. F., Croton, D., Bundy, K., et al. 2010, *ApJ*, 724, 915
- Jafaryazani, M., Newman, A. B., Mobasher, B., et al. 2025, *ApJ*, 986, 148
- Jafaryazani, M., Newman, A. B., Mobasher, B., et al. 2020, *ApJ*, 897, L42
- Jones, T., Wang, X., Schmidt, K. B., et al. 2015, *AJ*, 149, 107
- Ju, M., Wang, X., Jones, T., et al. 2025, *ApJ*, 978, L39
- Keating, S. K., Abraham, R. G., Schiavon, R., et al. 2015, *ApJ*, 798, 26
- Kobayashi, C. 2004, *MNRAS*, 347, 740
- Koekemoer, A. M., Aussel, H., Calzetti, D., et al. 2007, *ApJS*, 172, 196
- Kriek, M., Conroy, C., van Dokkum, P. G., et al. 2016, *Nature*, 540, 248
- Kriek, M., Price, S. H., Conroy, C., et al. 2019, *ApJ*, 880, L31
- Kroupa, P. 2001, *MNRAS*, 322, 231
- Kuntschner, H., Emsellem, E., Bacon, R., et al. 2006, *MNRAS*, 369, 497
- Kuntschner, H., Emsellem, E., Bacon, R., et al. 2010, *MNRAS*, 408, 97
- La Barbera, F., de Carvalho, R. R., Gal, R. R., et al. 2005, *ApJ*, 626, L19
- Larson, R. B. 1974, *MNRAS*, 166, 585
- Law, D. R., E. Morrison, J., Argyriou, I., et al. 2023, *AJ*, 166, 45
- Leja, J., Carnall, A. C., Johnson, B. D., Conroy, C., & Speagle, J. S. 2019, *ApJ*, 876, 3
- Li, H., Mao, S., Cappellari, M., et al. 2018, *MNRAS*, 476, 1765
- Lupton, R., Blanton, M. R., Fekete, G., et al. 2004, *PASP*, 116, 133
- Maiolino, R. & Mannucci, F. 2019, *A&A Rev.*, 27, 3
- Mann, A. W., Feiden, G. A., Gaidos, E., Boyajian, T., & von Braun, K. 2015, *ApJ*, 804, 64
- Martig, M., Bournaud, F., Teyssier, R., & Dekel, A. 2009, *ApJ*, 707, 250
- Martín-Navarro, I. 2016, *MNRAS*, 456, L104
- Martín-Navarro, I., Vazdekis, A., Falcón-Barroso, J., et al. 2018, *MNRAS*, 475, 3700
- Maseda, M. V., Lewis, Z., Matthee, J., et al. 2023, *ApJ*, 956, 11
- Matteucci, F. 1994, *A&A*, 288, 57
- McCracken, H. J., Milvang-Jensen, B., Dunlop, J., et al. 2012, *A&A*, 544, A156
- Mehlert, D., Thomas, D., Saglia, R. P., Bender, R., & Wegner, G. 2003, *A&A*, 407, 423
- Miller, T. B., van Dokkum, P., & Mowla, L. 2023, *ApJ*, 945, 155
- Miller, T. B., Whitaker, K. E., Nelson, E. J., et al. 2022, *ApJ*, 941, L37
- Moffat, A. F. J. 1969, *A&A*, 3, 455
- Muzzin, A., Marchesini, D., Stefanon, M., et al. 2013a, *ApJ*, 777, 18
- Muzzin, A., Marchesini, D., Stefanon, M., et al. 2013b, *ApJS*, 206, 8
- Naab, T., Johansson, P. H., & Ostriker, J. P. 2009, *ApJ*, 699, L178
- Nelson, E. J., Tacchella, S., Diemer, B., et al. 2021, *MNRAS*, 508, 219
- Nelson, E. J., van Dokkum, P. G., Förster Schreiber, N. M., et al. 2016, *ApJ*, 828, 27
- Newman, A. B., Ellis, R. S., Bundy, K., & Treu, T. 2012, *ApJ*, 746, 162
- Newman, A. B., Gu, M., Belli, S., et al. 2025, arXiv e-prints, arXiv:2503.17478
- Oke, J. B. & Gunn, J. E. 1983, *ApJ*, 266, 713
- Oser, L., Naab, T., Ostriker, J. P., & Johansson, P. H. 2012, *ApJ*, 744, 63
- Oser, L., Ostriker, J. P., Naab, T., Johansson, P. H., & Burkert, A. 2010, *ApJ*, 725, 2312
- Oyarzún, G. A., Bundy, K., Westfall, K. B., et al. 2019, *ApJ*, 880, 111
- Parikh, T., Saglia, R., Thomas, J., et al. 2024, *MNRAS*, 528, 7338
- Park, M., Belli, S., Conroy, C., et al. 2024, *ApJ*, 976, 72
- Pastorello, N., Forbes, D. A., Foster, C., et al. 2014, *MNRAS*, 442, 1003
- Pathak, D., Belli, S., & Weinberger, R. 2021, *ApJ*, 916, L23
- Peletier, R. F. & Valentijn, E. A. 1989, *Ap&SS*, 156, 127
- Peng, C. Y., Ho, L. C., Impey, C. D., & Rix, H.-W. 2010, *AJ*, 139, 2097
- Pérez-González, P. G., D'Eugenio, F., Rodríguez del Pino, B., et al. 2024, arXiv e-prints, arXiv:2405.03744
- Perna, M., Arribas, S., Marshall, M., et al. 2023, *A&A*, 679, A89
- Perrin, M. D., Long, J., Sivaramakrishnan, A., et al. 2015, *WebbPSF: James Webb Space Telescope PSF Simulation Tool*, Astrophysics Source Code Library, record ascl:1504.007
- Pipino, A., D'Ercole, A., Chiappini, C., & Matteucci, F. 2010, *MNRAS*, 407, 1347
- Pipino, A., D'Ercole, A., & Matteucci, F. 2008, *A&A*, 484, 679
- Pizzardo, M., Damjanov, I., Sohn, J., & Geller, M. J. 2025, arXiv e-prints, arXiv:2507.10675
- Poggianti, B. M., Moretti, A., Calvi, R., et al. 2013, *ApJ*, 777, 125
- Price, S. H., Kriek, M., Shapley, A. E., et al. 2016, *ApJ*, 819, 80
- Quilis, V. & Trujillo, I. 2013, *ApJ*, 773, L8
- Rodríguez-Gómez, V., Pillepich, A., Sales, L. V., et al. 2016, *MNRAS*, 458, 2371
- Sánchez-Blázquez, P., Forbes, D. A., Strader, J., Brodie, J., & Proctor, R. 2007, *MNRAS*, 377, 759
- Sánchez-Blázquez, P., Peletier, R. F., Jiménez-Vicente, J., et al. 2006, *MNRAS*, 371, 703
- Santucci, G., Brough, S., Scott, N., et al. 2020, *ApJ*, 896, 75
- Scoville, N., Aussel, H., Brusa, M., et al. 2007, *ApJS*, 172, 1
- Shen, L., Papovich, C., Matharu, J., et al. 2024, *ApJ*, 963, L49
- Slob, M., Kriek, M., Beverage, A. G., et al. 2024, *ApJ*, 973, 131
- Slob, M., Kriek, M., de Graaff, A., et al. 2025, arXiv e-prints, arXiv:2506.04310
- Smith, J. D. T., Armus, L., Dale, D. A., et al. 2007, *PASP*, 119, 1133
- Snyder, G. F., Cox, T. J., Hayward, C. C., Hernquist, L., & Jonsson, P. 2011, *ApJ*, 741, 77
- Speagle, J. S. 2020, *MNRAS*, 493, 3132
- Spilker, J. S., Bezanson, R., Weiner, B. J., Whitaker, K. E., & Williams, C. C. 2019, *ApJ*, 883, 81
- Spitoni, E., Vincenzo, F., & Matteucci, F. 2017, *A&A*, 599, A6
- Spolaor, M., Kobayashi, C., Forbes, D. A., Couch, W. J., & Hau, G. K. T. 2010, *MNRAS*, 408, 272
- Stringer, M., Trujillo, I., Dalla Vecchia, C., & Martínez-Valpuesta, I. 2015, *MNRAS*, 449, 2396
- Suess, K. A., Kriek, M., Price, S. H., & Barro, G. 2019a, *ApJ*, 877, 103
- Suess, K. A., Kriek, M., Price, S. H., & Barro, G. 2019b, *ApJ*, 885, L22
- Suess, K. A., Kriek, M., Price, S. H., & Barro, G. 2020, *ApJ*, 899, L26
- Suess, K. A., Kriek, M., Price, S. H., & Barro, G. 2021, *ApJ*, 915, 87
- Suess, K. A., Williams, C. C., Robertson, B., et al. 2023, *ApJ*, 956, L42
- Sybilska, A., Kuntschner, H., van de Ven, G., et al. 2018, *MNRAS*, 476, 4501
- Szomoru, D., Franx, M., van Dokkum, P. G., et al. 2013, *ApJ*, 763, 73
- Tacchella, S., Carollo, C. M., Förster Schreiber, N. M., et al. 2018, *ApJ*, 859, 56
- Tacchella, S., Carollo, C. M., Renzini, A., et al. 2015a, *Science*, 348, 314
- Tacchella, S., Dekel, A., Carollo, C. M., et al. 2016, *MNRAS*, 458, 242
- Tacchella, S., Lang, P., Carollo, C. M., et al. 2015b, *ApJ*, 802, 101
- Thomas, D., Greggio, L., & Bender, R. 1999, *MNRAS*, 302, 537
- Tinsley, B. M. 1979, *ApJ*, 229, 1046
- Trippodi, R., D'Eugenio, F., Maiolino, R., et al. 2024, *Spatially resolved emission lines in galaxies at $4 \leq z < 10$ from the JADES survey: evidence for enhanced central star formation*
- Trujillo, I., Cenarro, A. J., de Lorenzo-Cáceres, A., et al. 2009, *ApJ*, 692, L118
- Trujillo, I., Rudnick, G., Rix, H.-W., et al. 2004, *ApJ*, 604, 521
- Trussler, J., Maiolino, R., Maraston, C., et al. 2020, *MNRAS*, 491, 5406
- Valentino, F., Brammer, G., Gould, K. M. L., et al. 2023, *ApJ*, 947, 20
- van de Sande, J., Kriek, M., Franx, M., et al. 2013, *ApJ*, 771, 85
- van den Bosch, F. C., Aquino, D., Yang, X., et al. 2008, *MNRAS*, 387, 79
- van der Wel, A., Franx, M., van Dokkum, P. G., et al. 2014, *ApJ*, 788, 28
- van der Wel, A., Holden, B. P., Zirm, A. W., et al. 2008, *ApJ*, 688, 48
- van der Wel, A., Martorano, M., Häußler, B., et al. 2024, *ApJ*, 960, 53
- van Dokkum, P., Conroy, C., Villaume, A., Brodie, J., & Romanowsky, A. J. 2017, *ApJ*, 841, 68
- van Dokkum, P. G., Bezanson, R., van der Wel, A., et al. 2014, *ApJ*, 791, 45
- van Dokkum, P. G. & Franx, M. 2001, *ApJ*, 553, 90
- van Dokkum, P. G., Nelson, E. J., Franx, M., et al. 2015, *ApJ*, 813, 23
- van Dokkum, P. G., Whitaker, K. E., Brammer, G., et al. 2010, *ApJ*, 709, 1018
- Villaume, A., Conroy, C., Johnson, B., et al. 2017, *ApJS*, 230, 23
- Virtanen, P., Gommers, R., Oliphant, T. E., et al. 2020, *Nature Methods*, 17, 261
- Wellons, S., Torrey, P., Ma, C.-P., et al. 2015, *MNRAS*, 449, 361
- Wetzel, A. R., Tinker, J. L., & Conroy, C. 2012, *MNRAS*, 424, 232
- Whitaker, K. E., Kriek, M., van Dokkum, P. G., et al. 2012, *ApJ*, 745, 179
- White, S. D. M. 1980, *MNRAS*, 191, 1P
- Worthey, G. 1994, *ApJS*, 95, 107
- Wuyts, S., Cox, T. J., Hayward, C. C., et al. 2010, *ApJ*, 722, 1666
- Zhuang, Z., Leethochawalit, N., Kirby, E. N., et al. 2023, *ApJ*, 948, 132
- Zibetti, S., Gallazzi, A. R., Hirschmann, M., et al. 2020, *MNRAS*, 491, 3562
- Zolotov, A., Dekel, A., Mandelker, N., et al. 2015, *MNRAS*, 450, 2327
- Zolotov, A., Willman, B., Brooks, A. M., et al. 2010, *ApJ*, 721, 738

Appendix A: Wiggle correction algorithm

As discussed in Section 3.1, spatially-resolved *JWST* observations are affected by undersampling of the PSF. Algorithms to correct these wiggles in NIRSpec IFU data have been introduced in Perna et al. (2023) and in the WiCKED Python package (Dumont et al. 2025). However, at the time of writing, this study is the first one that tries to correct the wiggles in spatially-resolved NIRSpec-MSA spectra. Thus, we implement an algorithm that is heavily based on the ones presented in Perna et al. (2023) and WiCKED, but we combine and customize these routines for our specific case. We summarize the steps in our algorithm here.

We first fit the wiggles using the spectrum extracted from the row with the highest S/N. To obtain the shape of the wiggle, we mask strong emission lines. Then, we use the integrated spectrum as a reference spectrum and divide this from the brightest row, with both the reference and individual row spectra normalized by the value between 4480-4520 Å (see Slob et al. 2024). We break the wiggle spectrum up into small regions (non-uniform in length) that cover the entire wavelength range and use a sinusoidal function to model the wiggle in each chunk. We iterate this process to find both the best chunk sizes and best-fitting sinusoidal models by minimizing the χ^2 value over the entire wiggle spectrum. We divide this wiggle model from the spectral row to produce a corrected spectrum in the brightest row. For objects with a detector gap, we fit the wiggle on each side of the gap independently (if the spectrum is long enough for a wiggle to be detected visually).

For the subsequent spectral rows, we implement the Fourier transform algorithm from WiCKED to identify which rows contain a wiggle. In particular, for rows near the edges, the spectrum is dominated by noise and the S/N is too low to detect a wiggle. Additionally, there are certain brighter rows that are not as strongly affected by the undersampling and spectral rectification, and thus do not require wiggle correction. For the rows that contain wiggles, we use the chunks and wiggle model fit in the brightest row as a prior to constrain the wiggle in the remaining rows. We visually check the fits in each row. In cases where these priors do not produce a good fit, we re-fit the rows without a prior. Similar to the brightest row, we divide the wiggle model for each row out of each respective spectral row to obtain a corrected spectrum. We ensure that flux is conserved during the wiggle correction procedure. We show an example of the wiggles and our correction in Fig. A.1.

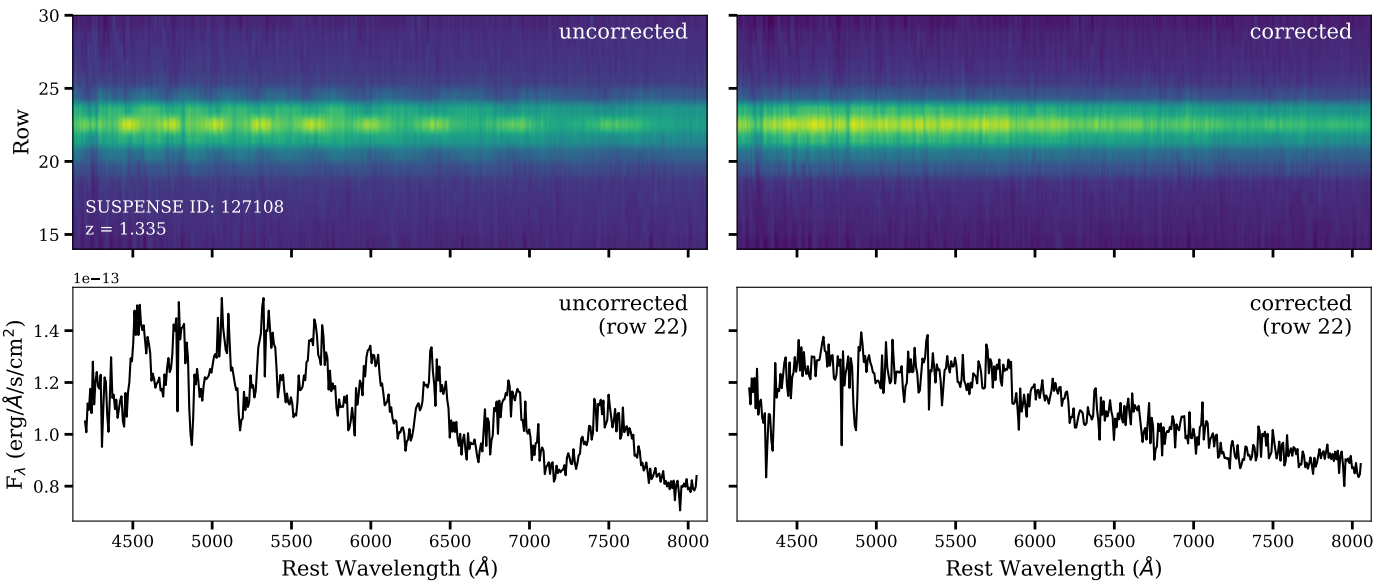


Fig. A.1. An example of the effect of our resampling noise correction for one object in our sample (object ID 127108). *Top:* 2D spectra. The uncorrected spectrum is shown on the left, where bright variations in the flux can be seen across the wavelength range. The corrected spectrum is shown on the right, where the flux is much more uniform across the wavelength range. *Bottom:* extracted 1D rows, median-binned by 3 pixels. In the left panel, we extract the brightest row from the uncorrected 2D spectrum. The bright variations in the flux seen in the top panel manifest as a sinusoidal flux variation in the 1D row. In the right panel, we extract the brightest row from the corrected 2D spectrum, where this sinusoidal flux variation has been removed.